Simultaneous conjugate observations of small-scale structures in Saturn's dayside ultraviolet auroras: Implications for physical origins

C. J. Meredith,[1] S. W. H. Cowley,[1] K. C. Hansen,[2] J. D. Nichols,[1] and T. K. Yeoman[1]

[1]   Small-scale features in Saturn's dayside UV auroras are examined using images obtained on 32 Hubble Space Telescope visits close to Saturn equinox when both northern and southern emissions were simultaneously observed, allowing their interhemispheric conjugacy to be investigated. Eastward-propagating patches in the dawn-to-noon sector were observed on ~70% of visits, which when present were nearly always observed both north and south. The patches were generally not closely conjugate, however, but typically displaced in local time by ~0.5–1 h, with maxima in one hemisphere falling near minima in the other. Averaged angular velocities were ~80% of rigid corotation, larger than plasma angular velocities reported in the outer magnetosphere to which the emissions are likely conjugate. We suggest the patches are associated with field-aligned currents of eastward-propagating ULF waves, specifically second harmonic Alfvén resonances with typical azimuthal wave numbers $m \approx 20$ and plasma rest frame periods ~80 min, plausibly driven by drift-bounce resonance with hot magnetospheric water ions. Transient dusk sector emissions of ~10–30 min duration were also observed on ~40% of visits, and found to be strictly nonconjugate, with enhancements in one hemisphere, north or south, being unaccompanied by enhancements in the other. We suggest an association with open flux tubes, and discuss one scenario where hemispheric symmetry is broken on newly opened flux tubes via the interplanetary magnetic field Y component, plausibly consistent with nonconjugate events north and south, preferential postnoon occurrence, and time scales of a few tens of minutes, though the expected relationship with the Y component remains to be established.

Citation: Meredith, C. J., S. W. H. Cowley, K. C. Hansen, J. D. Nichols, and T. K. Yeoman (2013), Simultaneous conjugate observations of small-scale structures in Saturn's dayside ultraviolet auroras: Implications for physical origins, *J. Geophys. Res. Space Physics*, *118*, 2244–2266, doi:10.1002/jgra.50270.

1.   Introduction

[2]   High-resolution observations of Saturn's UV emissions using the Hubble Space Telescope (HST) over the past ~15 years, and more recently using the Ultraviolet Imaging Spectrograph (UVIS) on the Cassini spacecraft, have shown the almost continuous presence of near-circular auroral ovals around each pole, centered typically near to ~16° colatitude in the south and ~15° in the north [e.g., *Gérard et al.*, 2004; *Badman et al.*, 2006; *Nichols et al.*, 2009; *Carbary*, 2012]. The difference in latitude is due to the quadrupole asymmetry of the internal magnetic field of the planet [e.g., *Burton et al.*,

2010]. The auroras are generally brighter on the dawn side of the planet than at dusk, sometimes contain substructures that sub-corotate relative to the planet, and exhibit dawnside brightenings and poleward expansions in response to solar wind induced magnetospheric compressions [*Clarke et al.*, 2005, 2009; *Grodent et al.*, 2005; *Bunce et al.*, 2006; *Gérard et al.*, 2006]. They are also known to respond in brightness and position to the phase of the "planetary period" oscillations that are ubiquitous in Saturn's magnetosphere [*Nichols et al.*, 2008, 2010a, 2010b]. Physically, the auroras result from the impact of ~10 keV electrons on the hydrogen upper atmosphere of the planet, resulting in H Lyman-α and H_2 Werner and Lyman band emissions [*Gérard et al.*, 2004, 2009]. The downward-directed electron fluxes most likely occur in regions of upward-directed field-aligned current associated with shears in the rotational flow, as sub-corotation on open field lines and in the outer magnetosphere gives way to near-rigid corotation in the middle and inner magnetosphere [*Cowley et al.*, 2004, 2008; *Bunce et al.*, 2008b; *Belenkaya et al.*, 2011]. In addition, a weak secondary UV oval has been observed centered on ~23° colatitude in the southern hemisphere, mapping to the middle and inner regions, possibly associated with scattering

[1]Department of Physics and Astronomy, University of Leicester, Leicester, UK.
[2]Department of Atmospheric, Oceanic and Space Sciences, University of Michigan, Ann Arbor, Michigan, USA.

Corresponding author: C. J. Meredith, Department of Physics and Astronomy, University of Leicester, Leicester LE1 7RH, UK. (cjm49@ion.le.ac.uk)

of trapped hot magnetospheric particles into the loss cone [*Grodent et al.*, 2010].

[3] In addition to the above large-scale morphology, small-scale features have also been observed in Saturn's UV auroras. *Gérard et al.* [2005] reported the presence of variable features in HST data occurring near the noon meridian that were suggested to be associated with the dayside cusp, and hence with solar wind coupling processes, while *Radioti et al.* [2011] examined UVIS data showing bifurcations in the noon and afternoon oval that they related to a similar physical origin. *Radioti et al.* [2009], using HST images also reported the occurrence of isolated auroral patches in the dusk sector which were shown to be transient in nature, brightening and decaying on ~10–30 min time scales. It was suggested on the basis of comparisons with near-contemporaneous in situ Cassini data that these could be formed by hot plasma injections within the magnetosphere, resulting in enhanced particle precipitation into the atmosphere. *Grodent et al.* [2011] further reported the occurrence in high-resolution UVIS pseudo-images of groups of small-scale auroral "spots" in the dawn and noon-sector oval. These were ~1000–3000 km in size (~1000 km corresponds to ~1° colatitude in the north-south direction), persisted for more than a few tens of minutes, and were found to rotate eastward at ~70% of rigid corotation. It was suggested that these structures might be formed by fluctuations in flow associated with Kelvin-Helmholtz (KH) waves at the magnetopause and/or boundary layer.

[4] It is evident that simultaneous conjugate observations of such features could provide key information about their physical origin. Both equatorially generated KH waves and plasma injections, for example, would produce emissions that are spatially conjugate in the two hemispheres, while cusp emissions involving open field lines need not generally obey strict conjugacy. Clearly near-simultaneous conjugate data cannot be obtained by UVIS, because north and south polar emissions are observed on differing parts of the Cassini orbit separated typically by many hours. In addition, only one polar region can usually be observed from Earth by HST due to the ~27° tilt of the planetary rotation axis, most recently the southern polar region between the 1995 and 2009 Saturn equinoxes. Near to equinox, however, the opportunity arises to obtain oblique but simultaneous conjugate images of Saturn's dayside auroras from Earth, an opportunity that was exploited in February–March 2009 by an intensive HST campaign when the Saturn sub-Earth latitude was very low ~−2.1° (vernal equinox was in mid-August 2009). Initial results were discussed by *Nichols et al.* [2009], who noted that while large-scale auroral characteristics generally varied in concert north and south, numerous examples of nonconjugate features were also present. In this paper we examine in more detail the small-scale auroral structures in this unique equinoctial data set, in particular the issue of their conjugacy, or otherwise, in the two hemispheres, and discuss implications for the physical origins of these features.

2. HST Equinoctial Campaign and Analysis of Auroral Images

[5] The HST Saturn equinoctial campaign used the Advanced Camera for Surveys (ACS) instrument, specifically employing the Solar Blind Channel (SBC) [*Nichols*

et al., 2009]. The ACS/SBC detector is a 1024×1024 Multi-Anode Microchannel Array with highest throughput in the FUV wavelength range 115–170 nm, and with an average resolution of ~0.032 arcsec pixel^{-1} such that the full field of view is ~35×31 arcsec^2 (a complete description is found in *Maybhate and Armstrong* [2010]). At Saturn's distance from Earth (8.39 AU during the campaign), this field of view is sufficient to encompass the whole of the planet plus a portion of the rings, thus allowing both northern and southern auroras to be observed simultaneously. The spatial resolution of the images, determined by the ACS/SBS point spread function (PSF) corresponds to ~2 detector pixels. In the noon-sector auroral region of principal interest here, this corresponds to ~400 km in the east-west direction (~0.1 h LT, local time), but to ~1500 km north-south (~1.5° latitude) due to the oblique view. For this reason we concentrate in sections 3 and 4 on the longitudinal structure of the oval emissions rather than the latitudinal. We note for comparison that the highest resolution auroral pseudo-images obtained by Cassini/UVIS have a spatial resolution of ~200 km both directions, though usually being less than this depending on the radial distance of the spacecraft [*Grodent et al.*, 2011].

[6] The campaign consisted of 32 one-orbit "visits" that took place between 23 January and 7 March 2009, with opposition between Saturn and Earth occurring on 8 March 2009. The visits were organized into seven groups termed A-G, each consisting of either six (A and B) or four (C-G) individual visits, thus termed A1 to A6, B1 to B6, and so on. However, for operational reasons planned visit A2 was delayed and undertaken out of sequence between visits A5 and A6, such that for clarity we have here relabeled visits A3-A5 and A2 as A′2-A′5 in correct time sequence. The vertical dashed lines in Figure 1, which spans the interval January-March 2009 (day of year (DoY) 1-90), show the times of each visit. The interval between each visit varies over a wide range of time scales, from successive HST orbits separated by ~1.5 h within groups, to intervals up to ~11 days between groups.

[7] The visit times in Figure 1 are superposed on modeled solar wind parameters at Saturn propagated from near-Earth observations using the MHD code of *Zieger and Hansen* [2008]. From top to bottom we show the solar wind number density, velocity, dynamic pressure, and field strength, together with the radial distance of Saturn's subsolar magnetopause obtained from the dynamic pressure using the *Kanani et al.* [2010] model. It can be seen that the modeled solar wind velocity is relatively low throughout the interval, ~350–400 km s^{-1}, while the number density is much more variable particularly toward lower values, thus leading to modest dynamic pressures typically below a few $\times 10^{-2}$ nPa, sometimes dropping as low as 10^{-3} nPa. Modeled subsolar magnetopause distances then typically lie in the range ~20–30 R_S, corresponding to HST groups A, B, E, and F, while sometimes expanding as far as ~30–40 R_S, as during groups C, D, and G. (R_S is Saturn's equatorial 1 bar radius, equal to 60,268 km.) Timing accuracies of the propagated data near Saturn opposition, determined by comparisons with in situ data, lie typically in the range ~0.5 to ~2 days [*Zieger and Hansen*, 2008; *Clarke et al.*, 2009; *Branduardi-Raymont et al.*, 2013], thus only marginally affecting these determinations.
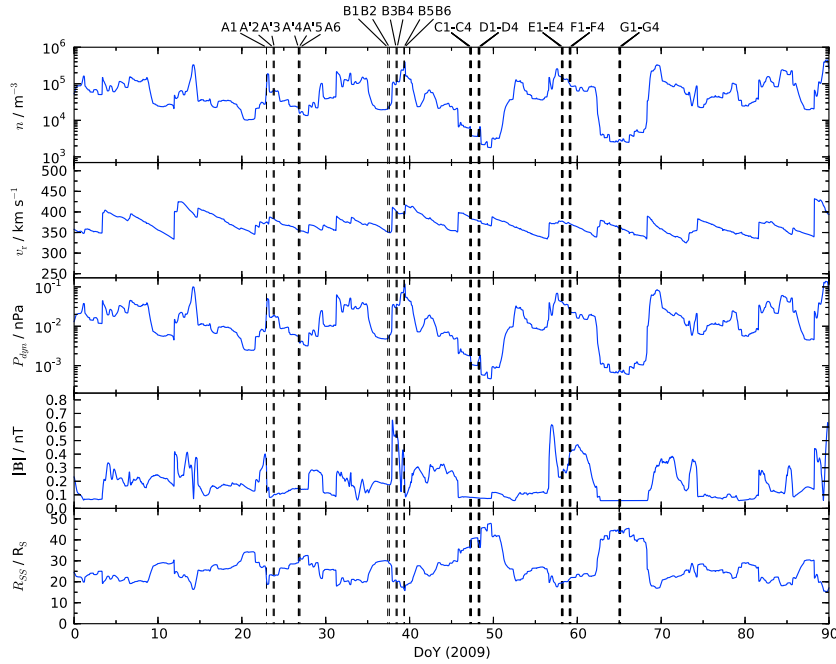
Figure 1. Plot showing modeled solar wind and magnetopause parameters at Saturn for the interval January–March 2009 (DoY 1–90). From top to bottom we show the solar wind number density (m^{-3}), velocity (km s^{-1}), dynamic pressure (nPa), and field strength (nT), together with the radial distance to the subsolar magnetopause (R_S). The solar wind parameters were propagated from Earth using the one-dimensional MHD model of *Zieger and Hansen* [2008], while the magnetopause distance was obtained from the dynamic pressure using the model of *Kanani et al.* [2010]. The superposed vertical dashed lines show the times of the 32 HST "visits" whose images are studied in this paper.

It may be noted that the campaign interval corresponds to the bottom of the recent deep and extended minimum in the solar cycle, with averaged sunspot numbers near to zero (see http://secchi.nrl.navy.mil/cactus/).

[8] During each ~40 min visit nineteen individual images were obtained each with 100 s exposure, except for visit G4 when seventeen images were obtained. The overall data set thus consists of 606 images. Two filters were also employed, F115LP and F125LP, covering the FUV wavelength ranges 115–170 nm and 125–170 nm, respectively. The former thus admits both H Lyman-α and H$_2$ Lyman/Werner band emission, while the latter excludes H Lyman-α, which is important when contamination from Earth's geocorona is likely. In groups A and B the first seven images in each visit were obtained using the F115LP filter, while the remaining twelve employed the F125LP filter. In groups C-G the F115LP filter was used throughout. The images were then subject to a pipeline reduction process involving calibration using relevant files obtained from the Space Science Telescope Institute, location of the planetary disc and scaling to a standard distance of 8.2 AU, and removal of reflected sunlight (see *Nichols et al.* [2009] for further details). Here we have also co-added the data from each pair of adjacent images to improve the counting statistics, though not for adjacent images in groups A and B that use different filters. This results in a final data set of 562 co-added images, 132 using the F125LP filter (groups A and B only), and 430 using the F115LP filter.

[9] The polar auroral data from each co-added image were then mapped onto latitude-longitude grids in each hemisphere,

simulating the view looking down onto the planet from the north in both hemispheres, with the images being clipped near the limb to avoid over-stretching as the view becomes increasingly oblique. The mapping assumes an auroral height of 1100 km above the 1 bar reference spheroid, corresponding to the peak in the emission height profile [*Gérard et al.*, 2009]. These mapped images represent the primary resource employed in this study, as discussed in the following sections.
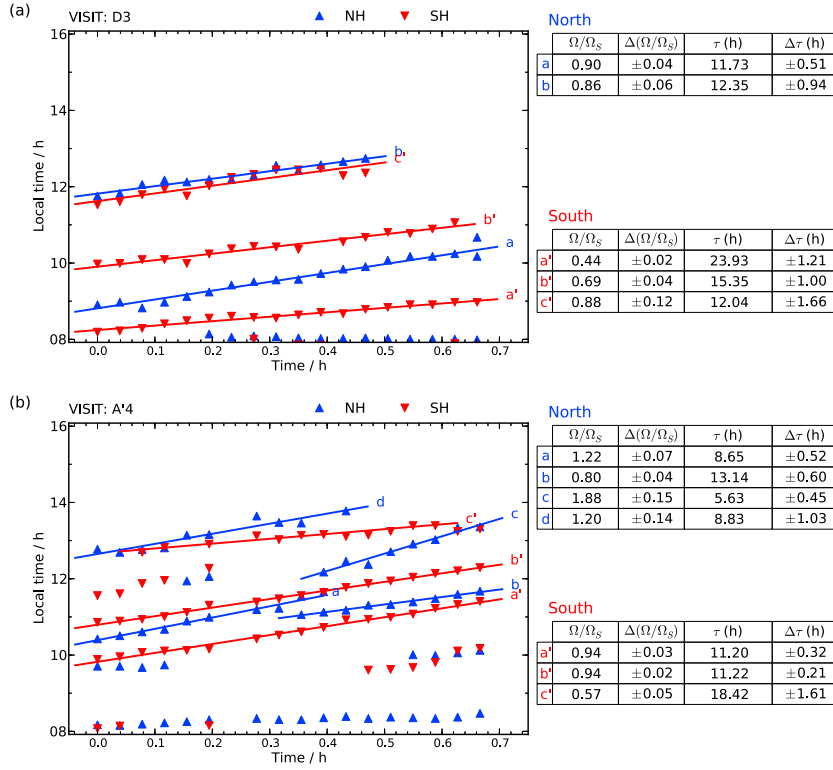
3. Auroral Patches in the Dawn Sector

3.1. Examples and Analysis Methods

[10] Figure 2 shows a representative set of images from visit D3 on 18 February 2009, where the four sets of plots display the northern and southern auroral emissions from co-added images 5, 9, 13, and 17, separated from each other by intervals of ~9 min. The visit and image number are shown at the top of each set, together with the center time of the data in the plot. The top two panels in each plot show polar strips containing the auroral emissions in the original reduced images for the northern (left) and southern (right) hemispheres, where the white dashed line shows the planetary limb. The log intensity scale is shown at the top of the figure, saturated red at 100 kR. The middle panels show the corresponding projected images, plotted for ease of comparison with noon at the bottom and dawn on the left in both hemispheres, such that the view is looking down from the north in each case (thus through the planet in the south). White dotted lines show colatitude circles at 10° intervals and LT meridians at 2 h intervals. The blue and red dotted circles show magnetically conjugate latitude bands
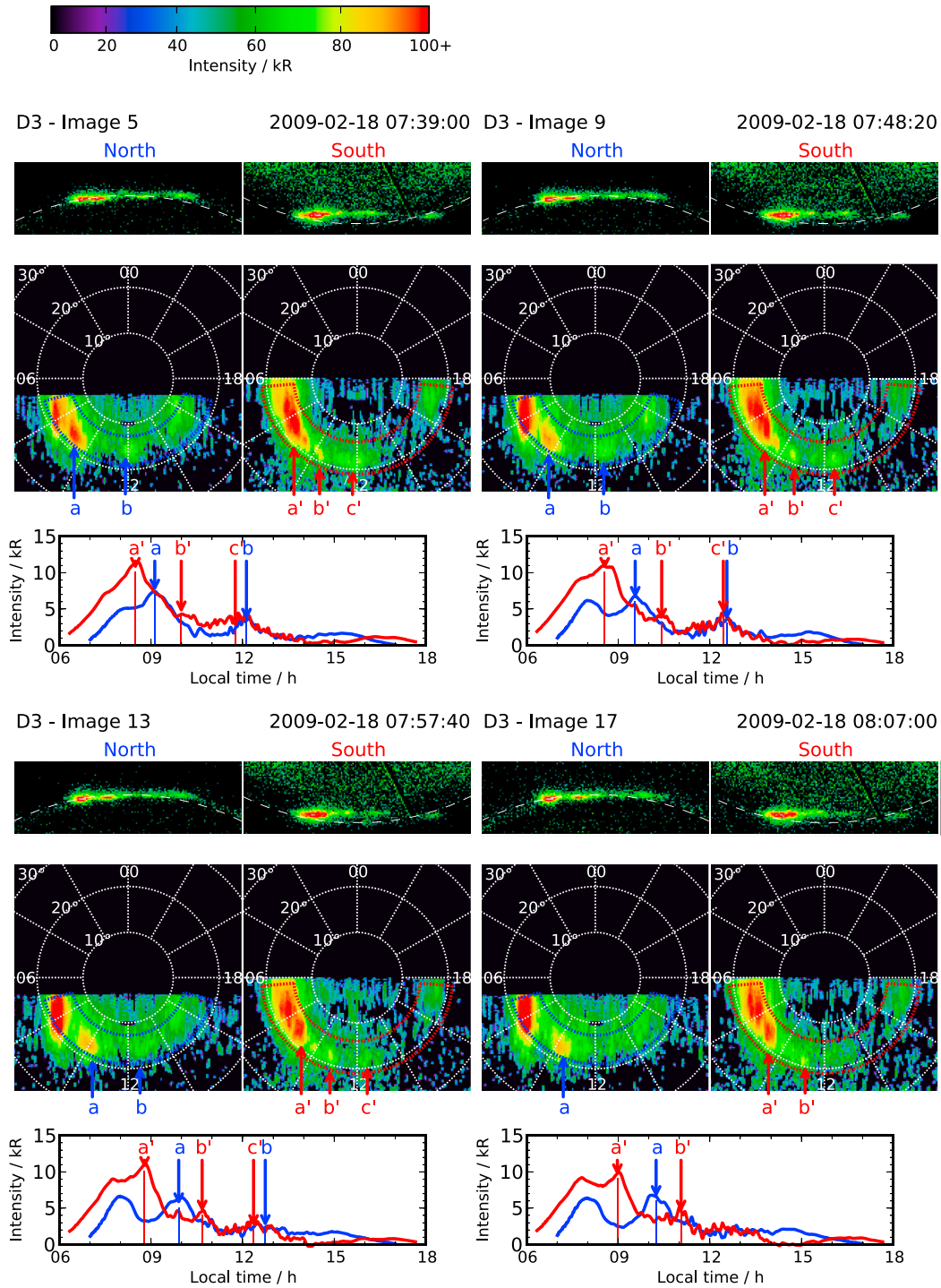
Figure 2. Saturn auroral observations from HST visit D3 on 18 February 2009, displaying data from co-added images 5, 9, 13, and 17, as indicated at the top of each plot set. The center times of the co-added images are also given, separated from each other by intervals of ~9 min. The top two panels in each set show polar strips containing the auroral emissions in the original reduced images for the northern (left) and southern (right) hemispheres, where the white dashed line shows the planetary limb. The intensity scale is shown at the top of the figure, saturated red at 100 kR. The middle panels in each set show the corresponding projected images, both plotted with noon at the bottom and dawn on the left. White dotted lines show co-latitude circles at 10° intervals and LT meridians at 2 h intervals, while the blue and red dotted circular segments in the north and south, respectively, show magnetically conjugate latitude bands that span the main emissions in both hemispheres. The lower panels in each set show the emission intensity in kR averaged in latitude over these bands in the north (blue) and south (red), to which a simple correction for limb brightening has been applied, and plotted versus LT. The lettered arrows in this panel mark the principal peaks in emission (other than the standing dawn arc), the positions of which are determined as indicated in section 3.1. The corresponding features in the images are also indicated by similarly lettered arrows.

(a) VISIT: D3 — NH (blue triangle), SH (red inverted triangle)

North

	Ω/Ω_S	$\Delta(\Omega/\Omega_S)$	τ (h)	$\Delta\tau$ (h)
a	0.90	±0.04	11.73	±0.51
b	0.86	±0.06	12.35	±0.94

South

	Ω/Ω_S	$\Delta(\Omega/\Omega_S)$	τ (h)	$\Delta\tau$ (h)
a'	0.44	±0.02	23.93	±1.21
b'	0.69	±0.04	15.35	±1.00
c'	0.88	±0.12	12.04	±1.66

(b) VISIT: A'4 — NH (blue triangle), SH (red inverted triangle)

North

	Ω/Ω_S	$\Delta(\Omega/\Omega_S)$	τ (h)	$\Delta\tau$ (h)
a	1.22	±0.07	8.65	±0.52
b	0.80	±0.04	13.14	±0.60
c	1.88	±0.15	5.63	±0.45
d	1.20	±0.14	8.83	±1.03

South

	Ω/Ω_S	$\Delta(\Omega/\Omega_S)$	τ (h)	$\Delta\tau$ (h)
a'	0.94	±0.03	11.20	±0.32
b'	0.94	±0.02	11.22	±0.21
c'	0.57	±0.05	18.42	±1.61

Figure 3. Plots showing the LT of principal maxima in the intensity-LT line plots (see Figure 2) plotted versus image time for the sequence of images obtained from a given visit. Blue triangles and red inverted triangles correspond to maxima in the north and south, respectively, and the image time is relative to the center time of the first co-added image in the visit. Least-squares linear fits to image-to-image sequences of maxima are also shown, whose gradients and corresponding rotation periods (with formal uncertainty estimates) are indicated on the right, identified by corresponding letters a, b, c, and a', b', c', and so on. The gradients are given as fractions of 10.56 h rigid corotation, corresponding to angular velocity Ω_S. Results are shown for (a) visit D3 (as in Figure 2), and (b) visit A 4 where the one-point data gap at ~0.23 h is due to the change in ACS/SBC filter, such that a co-added image is not formed at this time.

in the north and south, respectively, which encompass the bulk of the auroral emission in both hemispheres. The emission intensity (in kR) has then been averaged in latitude over each of these bands in LT strips 0.05 h wide, and is plotted versus LT in the panel beneath the images for both the northern (blue) and southern (red) hemispheres. These profiles have also been subject to a simple correction for limb brightening through multiplication by the cosine of the viewing angle to the local vertical [e.g., *Grodent et al.*, 2005].

[11] The overall auroral morphology in these images follows the usual pattern, with bright arc-like emissions at dawn and weaker forms at dusk in both hemispheres. However, it can also be seen that in addition to the quasi-steady dawn arc, patch-like emissions are observed between dawn and noon in both hemispheres, in general labeled a, b, c, and so on, in the north, and a', b', c' in the south, that yield similarly-labeled peaks in the intensity-LT line plots beneath the images. (The near-fixed peaks due to the quasi-steady dawn arcs are not so labeled, however.) Examination of the location of these patches and corresponding peaks from plot-to-plot in the figure shows consistent eastward motion in both hemispheres, as quantified below. As also shown below (section 3.2), such dawnside patches represent a very common feature in our data set, whose location in the oval, spatial scale, and motion are all similar to the small-scale

"spot" auroral structures previously identified in Cassini UVIS pseudo-images (albeit at greater spatial resolution in the best images) by *Grodent et al.* [2011]. The similarity is even more striking in the UVIS images presented in Figure 4 of the latter paper, which have a spatial resolution ~300–400 km, more comparable to that of the HST images employed here.

[12] If we newly examine the relation between features observed in the north and south, however, we see that while patches are indeed simultaneously present in both hemispheres, they are not generally closely conjugate, but instead are significantly displaced from each other in LT. In Figure 2, in particular, the maximum associated with patch a in the north clearly falls near-midway between patches a' and b' in the south throughout the interval, with peak emissions in opposite hemispheres being separated by ~1 h LT. The weaker near-noon maxima (labeled b in the north and c' in the south), however, are more nearly coincident.

[13] To quantify the relative locations of these patches, and their longitudinal motions, we have determined the LT position of the principal intensity maxima, and have followed them from image to image within each visit. The position of a maximum has been determined by considering the LT range in the intensity-LT line plot where the intensity lies continuously within 80% of a peak value, and calculating an intensity-weighted averaged LT within this range.
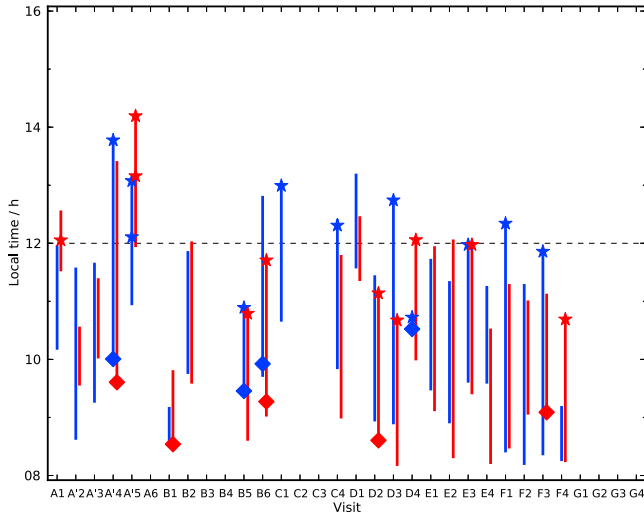
Figure 4. Plot showing the LT ranges on the vertical axis over which either single or multiple dawn auroral patches were observed during each HST visit, the latter being indicated sequentially in time along the horizontal axis. Blue bars correspond to the northern hemisphere and red to the southern. Diamonds indicate where patches were formed in the field of view during a given visit, and stars where they lost their identity. Where no such symbols are shown, the patches were either already present at the start of the visit, or had not disappeared at its end. For further discussion see section 3.2. The central dashed line indicates the noon meridian.

This procedure yields the positions of the maxima shown by the labeled vertical lines in the intensity-LT in plots Figure 2. We then plot the LT of these maxima versus image time for each of the images in a given HST visit, with results for visit D3 (as in Figure 2) being shown in Figure 3a. Blue symbols (triangles) correspond to maxima in the north, red (inverted triangles) o maxima in the south, and the time scale is relative to the center time of the first co-added image in each visit. It can be seen that the sequence of maxima from image-to-image corresponding to a given moving patch is very clear, displaying sequentially displaced peaks in the north and the south in the post-dawn sector, with more nearly coincident features near to noon. All these features drift rather steadily eastward with time over the interval, with the near-noon features losing their identity before the end of the visit as they propagate into the early afternoon sector. Least squares linear fits to these data then yield the overall angular velocities Ω of these motions, indicated (together with the formal uncertainty estimate) in the boxes to the right of the plot, labeled by the patch identifier letter. These angular velocities are expressed as fractions of rigid corotation with Saturn, where the rotation period of the latter is taken for definiteness to correspond to exactly 10.56 h (such that $\Omega_S \simeq 1.653 \times 10^{-4} \ rad \ s^{-1}$). Internal planetary periods of 10.54 h were inferred by *Anderson and Schubert* [2007] based on planetary oblateness, and 10.57 h by *Read et al.* [2009] based on considerations of Saturn's zonal winds, with the value taken here lying between these two. It can be seen that the rotation rates in this case correspond typically to $(\Omega/\Omega_S) \approx 0.7 - 0.9$, not dissimilar to the results of *Grodent et al.* [2011], though feature *a'* is significantly

slower. The corresponding rotation periods of the auroral features, typically ~12–15 h, are also given in the figure.

[14] A second more complicated example is shown in Figure 3b, taken from visit A'4, where the one-point data gap at ~0.23 h results from the change in ACS/SBC filter as mentioned in section 2. In this case interleaved northern and southern maxima are again evident in the prenoon sector, as seen in the sequence *a'*, *a*, *b'* with increasing LT in the first half of the visit. However, the picture is then complicated by a patch bifurcation event in the northern hemisphere that occurs around ~0.35 h, in which northern patch *a* splits into patches *b* and *c*. Patch *b* remains located between southern patches *a'* and *b'*, moving eastward more slowly than before (all modestly sub-corotating as in Figure 3a), while nonconjugate patch *c* moves with significantly super-corotating speed past *b'* into the postnoon sector. Patches *c'* and *d* are initially nearly colocated at ~13 h LT, similar to *c'* and *b* in D3 (Figure 3a), but then significantly diverge due to the sub-corotational motion of *c'*, and the modestly super-corotational motion of *d*.

3.2. Statistical Analysis

[15] We now provide an overview of the dawn patch phenomenon determined from all of the equinox campaign visits, analyzed in the same manner as in section 3.1. In Figure 4 we first show the LT ranges over which either single or multiple patches were observed, if any, during each visit, where the blue bar corresponds to the northern hemisphere and the red to the southern. It can be seen that patches are identified in 23 out of 32 visits, corresponding to ~72% of cases, such that it is a common phenomenon as indicated in section 3.1. Furthermore, in 22 out of these 23 cases, patches are identified in both hemispheres, such that when they occur, they usually occur both north and south. Of the nine visits in which patches were not identified, four correspond to the closely-spaced visits of group G extending over a ~5 h interval, and a further four to two closely-spaced pairs in B3-B4 and C2-C3. Comparison with Figure 1 does not suggest any consistent relation between the occurrence of these patches, or lack thereof, and the modeled state of expansion of the magnetosphere.

[16] Figure 4 also shows that the patches are primarily a dawnside phenomenon as indicated above, only rarely being observed beyond ~13 h LT. The diamonds and stars plotted on the vertical bars show where patches formed or lost their identity within a given visit, respectively. Where no such symbols are shown, patches were either already present at the start of the visit or had not disappeared at its end. Patch formation within the field of view centers near to ~9 h LT, though with many being present at earlier LTs at the start of the visits. Disappearances are centered near to ~12 h LT, the dashed horizontal line in the figure indicating noon. Diamonds drawn a short way along the bar (visit B6 north and south) indicate the center of a newly-formed patch that extended somewhat westward in LT, but, as in all cases, subsequently propagated eastward. Stars drawn part-way along the bars (visits A'2 and A'5 north and south) indicate the presence of multiple patches, one of which loses its identity at an earlier LT than one of the others.

[17] In Figure 5, we examine some typical properties of the patches. In Figure 5a, we consider the LT extent of individual patches, defined here to be the width within which
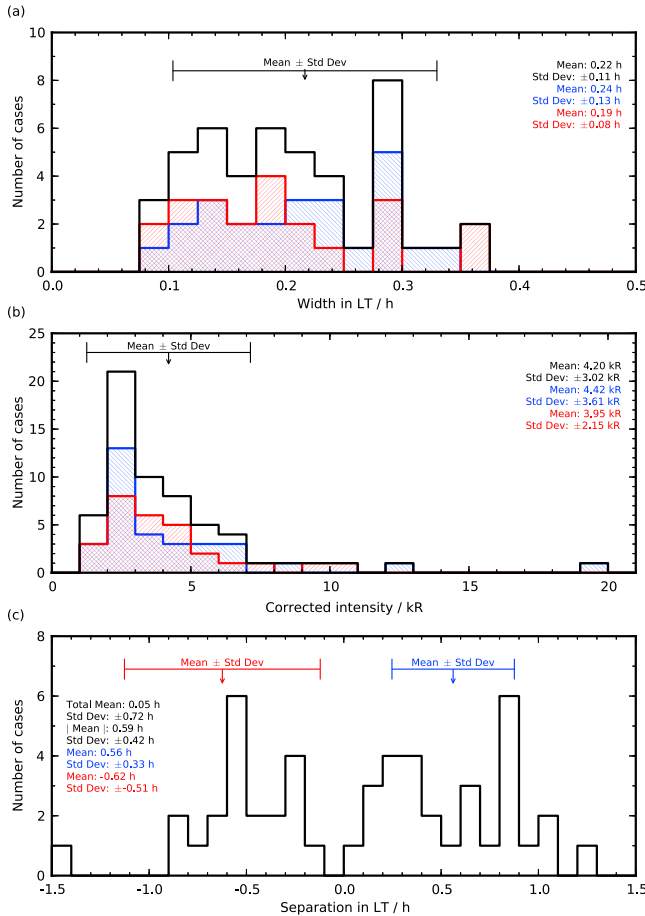
Figure 5. Histograms showing overall properties of the dawn auroral patches determined from the ensemble of equinox campaign visits. (a) The LT extent of individual patches, defined as the width within which the intensity remains above 80% of the peak value in the intensity-LT line plots, with values being averaged over all the images within a visit over the lifetime of the patch. Blue (downward hatching left to right) corresponds to northern patches, red (upward hatching left to right) to southern, and black to the overall data set. Mean values and standard deviations of these distributions are given numerically in the panel, as well as being indicated for the overall distribution by the vertical arrow and horizontal bar. (b) A corresponding histogram of peak limb-brightening corrected emission intensities (kR) similarly averaged over the lifetime of a patch on a given visit. (c) The LT displacement between adjacent pairs of patches in the northern and southern hemispheres, determined from the mean displacements of the linear fits (e.g., Figure 3) over the intervals of time when both patches were present. Positive values correspond to the northern patch being earlier in LT than the southern, and negative values vice versa, with all successive patch pairs being represented.

the intensity remains above 80% of the peak value in the intensity-LT plots, representing the width of the brightest central region of a patch, generally lying within a more extended but less well-defined region of emission. Values have been averaged over the lifetime of an individual patch within a given visit to produce the histograms shown, blue corresponding to northern patches, red to southern, and

black to the overall data set. No significant difference is observed between the north and south (see the statistical data within the figure panel), the overall mean and standard deviation (SD) being 0.22 ± 0.11 h LT. Overall, the distribution of widths spans from ~0.08 h LT, essentially the instrument PSF, to ~0.37 h LT, equivalent to ~4.5 times the PSF. This distribution also corresponds to a range of east-west distances from the ~400 km resolution limit up to ~2000 km, with the mean value corresponding to ~1000 km. These scales are thus comparable to the ~1000–2000 km scales of the auroral "spots" previously studied by *Grodent et al.* [2011]. Figure 5b shows a corresponding histogram of peak limb-brightening corrected emission intensities similarly averaged over the patch lifetime, typical values extending from ~2 to ~7 kR. These values are somewhat smaller than the ~10–30 kR range for individual "spots" quoted by *Grodent et al.* [2011], likely as a result of the latitudinal averaging undertaken here.

[18] Figure 5c newly addresses the issue of patch conjugacy. Here we show the LT displacement between adjacent pairs of patches in the northern and southern hemispheres, determined from the mean displacements of the linear fits (such as those shown in Figure 3) over the intervals of time when both patches were present. A positive value corresponds to the northern patch being at an earlier LT than the southern, and a negative value vice versa, with all successive patch pairs being represented. If the patches were an essentially conjugate phenomenon, the distribution would be strongly peaked near to zero displacement, with corresponding patches lying within ~±0.2 h LT of each other according to the above width determinations. The histogram in Figure 5c shows that very few patch pairs are "conjugate" within this limit, however, with observed separations typically being more than double this, extending up to ~±1 h LT. Rather, the distribution of separations is distinctly bi-modal between positive and negative values, indicating a preference for longitudinally displaced peaks north and south, such as those shown in Figures 2 and 3. The means and SDs of the positive and negative values taken separately are 0.56 ± 0.33 and -0.62 ± 0.51 h LT, respectively. However, roughly equal numbers of positive and negative values are represented in the plot (29 positive and 21 negative), indicating no significant preference for patches in the north to lead patches in the south or vice versa. The mean and SD of the distribution overall is 0.05 ± 0.72 h LT, consistent with zero.

[19] Figure 6a shows histograms of the dawn patch rotation angular frequencies Ω normalized to Ω_S as above, determined from linear fits such as those shown in Figure 3, while for ease of comprehension Figure 6b shows the same data in terms of rotation periods. Blue again corresponds to northern patches, red to southern, and black to the overall distribution. The distributions are seen to be very broad in both hemispheres, spanning $(\Omega/\Omega_S) \approx 0.3 - 2$, corresponding to periods to ~5–30 h. The purple arrow indicates near-rigid corotation with the planet at the period of 10.56 h as discussed above, while the orange arrow emphasizes that the periods of the rotating "planetary period" oscillations in Saturn's magnetosphere, ~10.6–10.8 h [e.g., *Andrews et al.*, 2012], are also almost the same as rigid corotation on this scale. The histograms show that while a small fraction of the patches
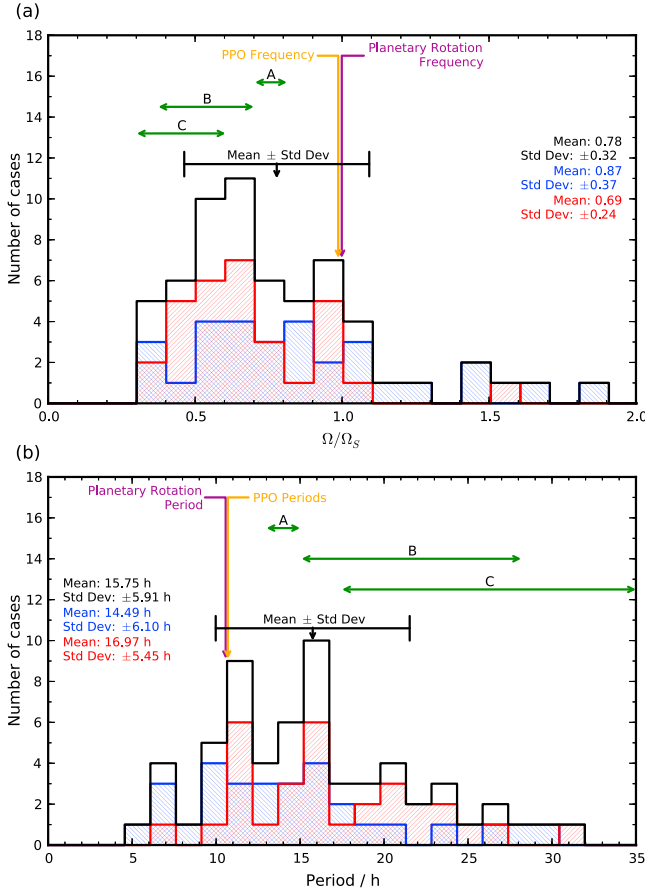
Figure 6. Histograms of (a) dawn patch normalized angular velocities, and (b) corresponding rotation periods, determined from linear fits to the image-to-image patch position determinations such as those shown in Figure 3. The angular velocities are normalized to the planetary angular velocity, taken to correspond to a period of exactly 10.56 h. Blue corresponds to northern patches, red to southern, and black to the overall distribution, as in Figure 5. The overall mean value and standard deviation is again shown by the vertical black arrow and horizontal bar. The purple arrow indicates the planetary rotation frequency/period, while the orange arrow indicates the frequency/period of the rotating "planetary period" oscillations, which is essentially the same on this scale. The green horizontal bars indicate the range of plasma rotation angular velocities/periods inferred from Cassini ion velocity measurements in differing equatorial radial ranges. Bar A corresponds to the results of *Wilson et al*. [2009] for 6–10 R_S, B to *Thomsen et al*. [2010] for 13–17 R_S, and C to *Arridge et al*. [2011] for 18–21 R_S.

(~20%) are observed to super-corotate, most of these corresponding to bifurcation events such as that shown in Figure 3b, the majority significantly sub-corotate. The overall mean and SD of the patch normalized angular velocity is $(\Omega/\Omega_S) \approx 0.78 \pm 0.32$ (the standard error of the mean being ± 0.04), while the mean and SD of the rotation period is 15.8 ± 5.9 h. Again, no significant differences within the uncertainties are observed between the separate northern and southern values, as given in the figure.

[20] It is of central physical interest to compare the patch angular frequencies with those of the thermal plasma measured in situ within the magnetosphere. Magnetic models indicate that the dayside auroras map to the outer part of the magnetosphere between the outer ring current and the magnetopause [*Belenkaya et al*., 2011], typically, say, to radial distances ~20 R_S when the magnetosphere is reasonably expanded [*Bunce et al*., 2008a], as seems appropriate to most of the interval examined here according to Figure 1. The green horizontal bars in the upper parts of the panels in Figure 6 show the plasma rotation angular frequencies/periods derived from Cassini equatorial ion velocity measurements in three recent studies spanning radial ranges at increasing distance. Bar A from *Wilson et al*. [2009] corresponds to the radial range 6–10 R_S in the dayside magnetosphere, mapping to lower latitudes than the main auroral oval, where $(\Omega_p/\Omega_S) \approx 0.7 - 0.8$ with periods ~13–15 h. These values are seen to be comparable to the mean patch values, though spanning a much narrower range. Bar B corresponds to the results of *Thomsen et al*. [2010] at larger equatorial distances of 13–17 R_S, encompassing a wide range of LTs including the dayside, that cover a broader and lower range of values $(\Omega_p/\Omega_S) \approx 0.4 - 0.7$, corresponding to periods ~15–26 h. These values are seen to span the lower range of auroral patch angular velocities, with a mean value at the larger distances of $(\Omega_p/\Omega_S) \approx 0.5$, rather lower than the mean angular velocity of the patches. Bar C then corresponds to the results of *Arridge et al*. [2011] at 18–21 R_S near Titan's orbit, which indicates a similarly broad range of values $(\Omega_p/\Omega_S) \approx 0.3 - 0.6$, corresponding to periods ~18–35 h, centered on an even smaller median value of $(\Omega_p/\Omega_S) \approx 0.4$. Overall, these results suggest typical plasma angular velocities $(\Omega_p/\Omega_S) \approx 0.4 - 0.5$ in the region to which the patches likely map in the outer magnetosphere, compared with mean angular velocities of $(\Omega/\Omega_S) \approx 0.8$ for the patches themselves. We thus infer that the patches typically propagate eastward relative to the plasma at modest angular velocities, as must certainly be the case for the fastest near-rigidly rotating and super-corotating patches.

4. Dusk Sector Transients

4.1. Examples

[21] We now turn to the phenomenon of dusk sector transients previously studied by *Radioti et al*. [2009], and in Figure 7 show a set of images from visit C4 in essentially the same format as Figure 2, although the optimized emission color-scale has now been saturated red at 60 kR as indicated at the top of the figure. Eastward-moving nonconjugate auroral patches separated by ~1 h LT are again present in the dawn sector, while here we instead focus on emissions in the dusk sector. Examining the northern hemisphere data, it can be seen that the emission brightens substantially at latitudes modestly higher than that of the dawn patches over a broad postnoon sector centered near ~15 h LT between images 5 and 9, producing peak *b* in the intensity-LT line plot for the latter image. The patch remains bright in image 13, though of diminished intensity, and then fades significantly in image 17. Examination of all the images in the visit shows that the lifetime of the transient emission is ~20 min, typical of the similarly-located transient events examined by
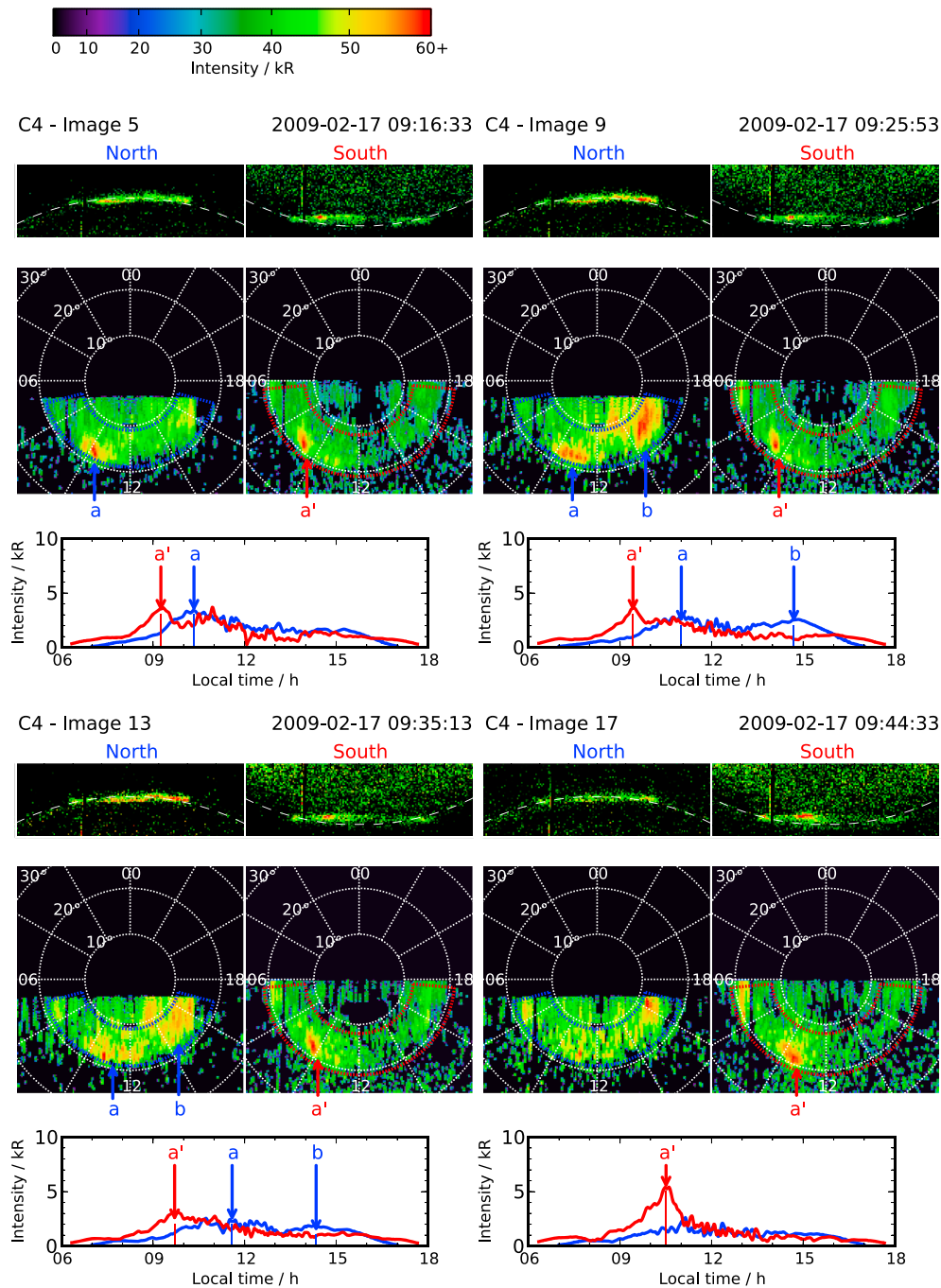
Figure 7. Auroral observations from HST visit C4 on 17 February 2009, in the same format as Figure 2, except that the emission intensity color scale is now saturated red at 60 kR as indicated at the top of the figure.

Radioti et al. [2009]. Newly examining the conjugate emissions in these images, however, it can be seen that no related enhancement occurred at all in the southern hemisphere, an unexpected finding that will be shown below to be a general property of these events.

[22] In Figure 8a, we show the LT of the auroral intensity maxima versus time for visit C4 in the same format as Figure 3, together with linear fits to the clear long-lived tracks. The dawn-side tracks again show the presence of nonconjugate patches in both northern and southern hemispheres propagating eastward. The near-stationary peak of dusk transient b in the northern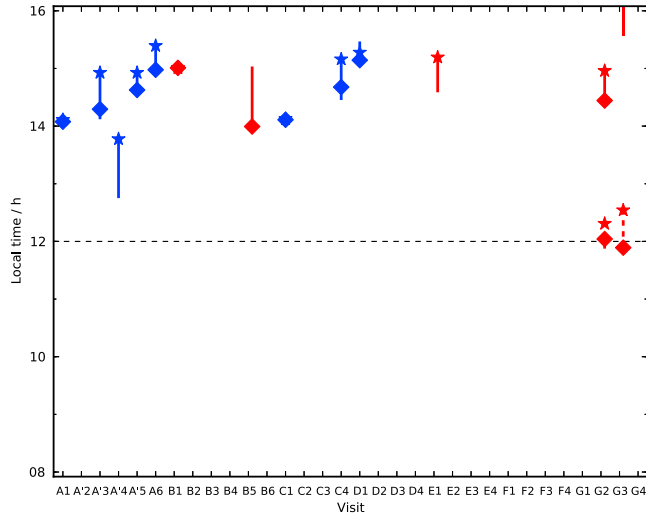 hemisphere is also evident for ~20 min near ~15 LT, with no corresponding southern feature. The linear fit to these data indicate an overall eastward drift at $(\Omega/\Omega_S) \approx 0.45 \pm 0.51$, consistent with zero. A second example is shown in Figure 8b for visit G2. Unusually in this case, no dawn patches are present in either hemisphere in conformity with Figure 4, while two patches are present in the southern hemisphere only, patch a' which is near-stationary close to noon with $(\Omega/\Omega_S) \approx 0.34 \pm 0.12$, and patch b' which is present for ~10 min centered near ~15 LT, which travels eastward at a super-corotational angular velocity $(\Omega/\Omega_S) \approx 1.72 \pm 0.36$ corresponding to a rotation period of ~6 h.
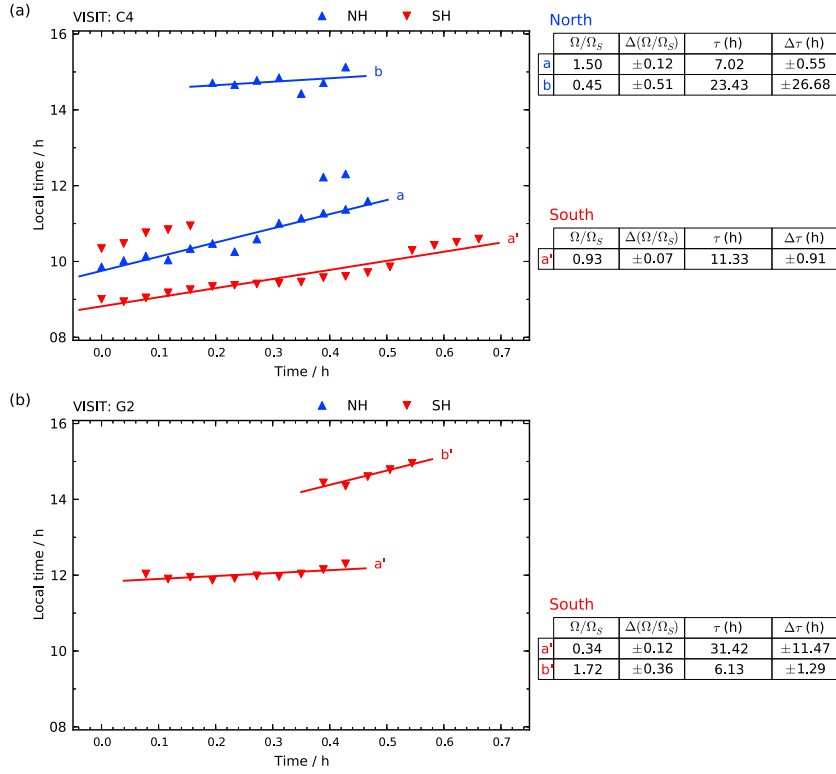
Figure 8. Plots showing the LT of principal maxima in the intensity-LT line plots, plotted versus image time for (a) visit C4 (as in Figure 7), and (b) visit G2, in the same format as Figure 3. Linear fits are shown to the data for the clear long-lived tracks.
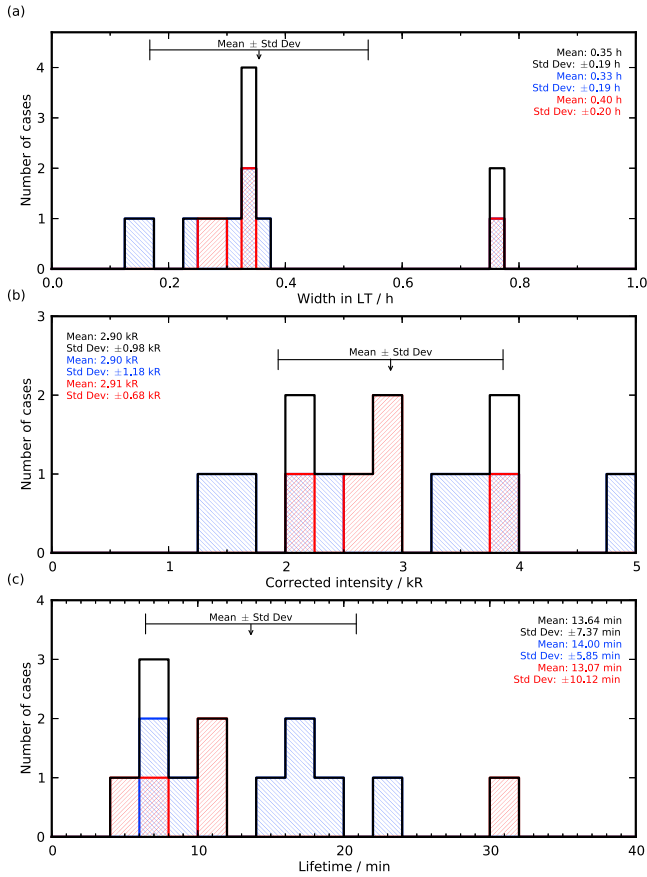
4.2. Statistical Analysis

[23] We now provide an overview of the dusk transient phenomenon determined from all of the equinox campaign data, and begin in Figure 9 by showing the occurrence and LT extent of the phenomenon for all of the visits in the same format as Figure 4. Dusk patches were observed in 13 out of 32 visits, corresponding to ~41% of cases, showing that it is a common phenomenon, but does not occur as frequently as the dawn sector patches. The events are also seen to be well-distributed throughout the data set, with at least one event occurring in each group of visits, except for group F where no dusk patches were observed over a ~5 h interval. Comparison with Figure 1 again does not suggest a clear relation between the occurrence of these transients and the modeled state of the magnetosphere. Most importantly, however, it is seen that although these events can be observed in both northern and southern hemispheres with roughly equal frequency within the small overall numbers involved, in no cases was a corresponding event observed in the conjugate hemisphere.

[24] The increased prevalence of diamonds and stars in Figure 9 compared with Figure 4 results from the short-lived nature of the dusk transient events compared with the dawn patches, such that we generally see both the formation (diamonds) and decay (stars) of the dusk events within a given visit. The mean location of formation is found to be ~14.5 h LT, while the mean location of decay is at ~15 h LT. Two single-hemisphere (southern) transient events are also observed close to noon on consecutive visits G2 and G3, marked by the dashed lines. Although their properties are similar to the more typical midafternoon events, it is not completely evident whether these form part of the same phenomenon, or whether they represent an additional rarer noon transient phenomenon. It may be noted from Figure 1 that these visits occurred during an extended interval of unusually low modeled dynamic pressure and consequent magnetospheric expansion (this conclusion not being affected by

Figure 9. Plot showing the LT ranges on the vertical axis over which dusk transient auroral patches were observed during each HST visit, the latter being indicated sequentially in time along the horizontal axis. The format is the same as for Figure 4.

Figure 10. Histograms showing overall properties of dusk auroral transients determined from the ensemble of equinox campaign visits, in a similar format to Figure 5. (a) The LT extent of individual transients, defined as the width within which the intensity remains above 80% of the peak value in the intensity-LT line plots, with values being averaged over all the images within a visit over the lifetime of an event. (b) A corresponding histogram of peak limb-brightening corrected emission intensities (kR) similarly averaged over the lifetime of the event. (c) A histogram of the lifetime of the dusk transients, determined as the duration over which the event can be identified by a clear peak in the intensity-LT line plots.

the range of timing uncertainties in the modeled parameters mentioned in section 2).

[25] In Figure 10, we examine some typical properties of the dusk transient events, determined in a similar way and shown in a similar format to the dawn patch properties in Figure 5. The parameters of the two noon transients from visits G2 and G3 have been excluded in this figure. In Figure 10a, we show a histogram of the LT width of the transient auroras averaged over their lifetime, whose mean and standard deviation are found to be 0.35 ± 0.19 h LT, respectively, with no significant difference between transients observed in the northern and southern hemispheres. These widths are thus somewhat larger than those of the dawn patches, which according to Figure 5 extend on average 0.22 ± 0.11 h in LT. Figure 10b similarly shows a histogram of peak limb-corrected emission intensities averaged over the patch lifetime, with a mean value and standard deviation of 2.9 ± 1.0 kR, similar to, but slightly smaller than, the

mean value of 4.2 ± 3.0 kR for the dawn patches. Figure 10c then shows a histogram of the lifetime of these events, spanning a range from ~6 to ~30 min, but with an overall mean and standard deviation of 13.6 ± 7.4 min. We note that these values are very similar to the range of ~7 to 30 min quoted by *Radioti et al.* [2009], though the intensities given above are somewhat less than the ~10 kR quoted by these authors, again possibly due to latitudinal averaging.

[26] In Figure 11, we show the angular frequency and rotation periods of the dusk transients determined from the linear fits to the image-to-image peak emission positions, as illustrated in Figure 8. Despite the smaller number of examples and the shorter lifetimes compared with the dawn patches, the distribution of values is even broader, spanning events that are essentially stationary in LT over their lifetime as for visit C4 shown in Figures 7 and 8a, and those that appear to super-corotate up to ~4 times the planetary angular velocity. Notwithstanding the breadth of the distribution, however, none of the dusk transients are found to move significantly westward against planetary rotation.
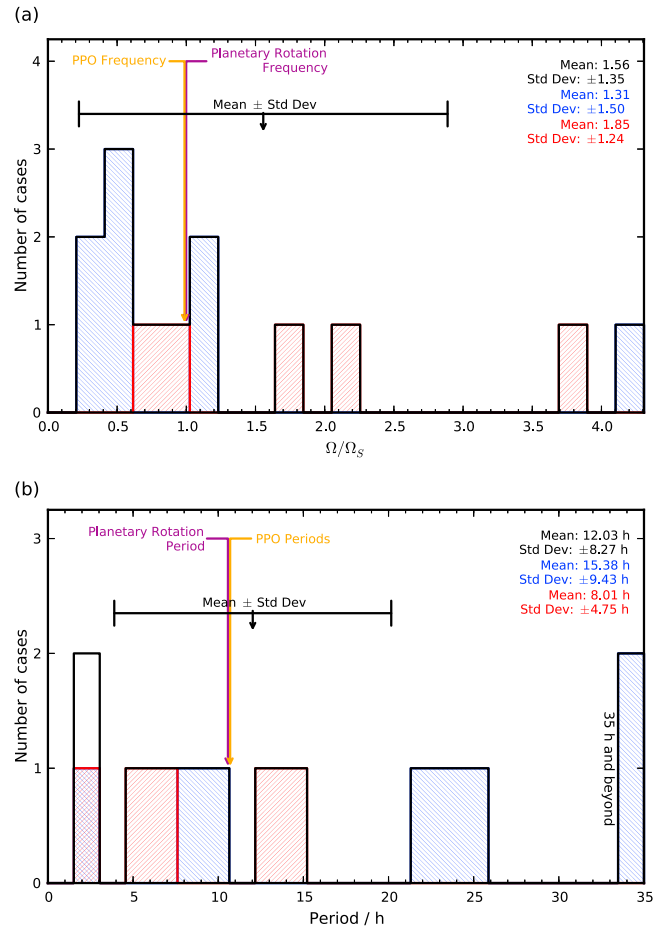
Figure 11. Histograms of (a) dusk transient normalized angular velocities, and (b) corresponding rotation periods, determined from linear fits to the image-to-image patch position determinations such as those shown in Figure 3. The format is similar to Figure 6.

5. Physical Origin of Dawn Sector Patches

5.1. Relevance of the Kelvin-Helmholtz Instability

[27] We now consider the physical origin of the auroral phenomena discussed above, beginning with the eastward-propagating dawn patches. *Grodent et al.* [2011] suggested that such small-scale auroral structures might be caused by KH waves occurring at the outer boundary of the magnetosphere, either at the magnetopause or in the adjacent boundary layer, specifically through the currents that couple the resulting perturbed plasma flow with the ionosphere. Alternatively, ULF field line resonances (FLRs) can be excited within the magnetosphere by such boundary wave sources, which similarly couple to the ionosphere [e.g., *Southwood*, 1974; *Southwood and Hughes*, 1983]. It is evident, however, that a KH source is inconsistent with the patch properties determined in this study, both with regard to their interhemispheric symmetry, and to their azimuthal propagation. We briefly discuss each in turn.

[28] The KH instability operates principally in the magnetospheric equatorial region (see, e.g., *Desroche et al.* [2012] in the case of Jupiter), the effects of which are transmitted along the field to the ionosphere by Alfvén waves carrying field-aligned currents. The field perturbations produced by the equatorial vortical flows associated with the instability are perforce in opposite directions on either side of the equator, a configuration we refer to as being of "odd" symmetry, and hence so are the field-aligned currents. A relevant discussion is given, e.g., by *Masters et al.* [2010]. Enhanced auroral emissions are expected to be associated with downward electron acceleration in regions of field-aligned current directed upward with respect to the ionosphere, which with the above "odd" field symmetry implies auroral patches that are conjugate in the two hemispheres. This is directly contrary to the observations presented in section 3, illustrated in Figures 2 and 3, which show that patches in the two hemispheres are characteristically displaced in longitude, with maxima in one hemisphere being located near-centrally between maxima in the other. This requires instead that the magnetic perturbations and field-aligned currents associated with the patches have the same direction on either side of the equator, i.e., have "even" symmetry, and are thus oppositely-directed with respect to the ionosphere in conjugate hemispheres. Exactly the same issue concerns the FLRs that might be excited inside the magnetosphere by coupling to KH waves on the boundary. Under near-equinoctial conditions of north-south symmetry in the magnetosphere, a source of "odd" symmetry on the boundary such as KH waves can excite "odd" mode FLRs inside the magnetosphere, principally the fundamental mode, but cannot excite "even" mode FLRs such as is required by our observations. We note that in both of the two terrestrial cases in which a magnetospheric ULF wave has been directly linked through a FLR with a KH wave at the boundary, the ULF wave has indeed been inferred to be in the fundamental mode [*Rae et al.*, 2005; *Agapitov et al.*, 2009].

[29] Turning now to the azimuthal propagation characteristics of the patches, we note that unstable KH waves driven by flow shear at a boundary propagate at a speed which is intermediate between the speeds on either side of the boundary. In the context of Saturn's dayside magnetopause in which the magnetospheric plasma sub-corotates at ~100 km s^{-1} adjacent to the boundary [*Thomsen et al.*, 2010; *Arridge et al.*, 2011; *Wilson et al.*, 2012], while the magnetosheath plasma flows tailward from the subsolar region at generally comparable speeds, the implication is that KH waves in the prenoon sector perforce propagate at all points at an eastward speed that is less than or equal to the plasma speed inside the boundary. A corresponding angular velocity would also be imposed on any FLRs driven inside the magnetosphere by KH waves. This is again contrary to the properties of the dawn patches, which as shown in section 3.2 and Figure 6, rotate eastward at a mean angular velocity which is considerably in excess of the plasma angular velocity in the outer magnetosphere, ~ 0.8 Ω_S compared with a plasma angular velocity implied by the above flow speed of ~ 0.4 Ω_S. As indicated in section 3.2, the field perturbations and currents associated with the patches thus propagate eastward relative to the plasma, rather than westward as required by a KH source.

[30] More specifically, growing KH modes are stationary in the frame in which the mass fluxes of the plasma (mass density times flow speed) are equal and opposite on either side of the boundary [e.g., *Southwood*, 1978]. At the dayside boundary at Saturn the mass densities are comparable on either side, though dominated by protons in the magnetosheath and water ions in the magnetosphere, so that the speed of the growing modes will be approximately the mean of the two flow speeds. If so, KH waves in the near-noon region where the magnetosheath flow is small will propagate eastward at half the speed of the magnetospheric plasma inside the boundary, i.e., at ~0.2 Ω_S according to the above discussion. The eastward propagation then slows at earlier LTs around the boundary, to near zero where the tailward magnetosheath speed reaches ~100 km s^{-1}. According to simple magnetosheath models this would occur near ~10 h LT [e.g., *Stahara et al.*, 1989], in agreement with the results of *Wilson et al.* [2012]. At still earlier LTs the propagation then reverses to tailward. We note in this context that in a study of magnetopause boundary normal deflections, *Masters et al.* [2012a] found that these were consistent with tailward propagation in ~80% of cases, both at dawn and dusk. By contrast, the dawn auroral patches studied here move consistently eastward at all LTs later than ~8 h LT covered by the HST images, with relatively constant angular velocities over their observed lifetimes (e.g., Figures 3 and 8) averaging ~ 0.8 Ω_S.

5.2. Relevance of Drift-Bounce Resonance Instability

[31] These considerations thus show conclusively that the dawn patch phenomenon is not driven by KH waves at the boundary, nor by FLRs excited by them within the magnetosphere. A second possibility, however, is that ULF FLRs can be driven within the magnetosphere by resonant interactions with trapped magnetospheric particles. Such waves are known to commonly occur within the Earth's magnetosphere, with modes of "even" magnetic and current symmetry as indicated by our observations (principally second harmonic waves) being driven by drift-bounce resonance with trapped ring-current ions [e.g., *Hughes et al.*, 1978; *Yeoman and Wright*, 2001; *Wright et al.*, 2001; *Baddeley et al.*, 2002, 2005]. Here we therefore make an initial assessment of the relevance of this mechanism to the dawn patch phenomenon at Saturn, starting with the conditions for resonance.

[32] The condition for local drift-bounce resonance derived by *Southwood et al.* [1969] is given by

$$\omega - m\omega_d = N\omega_b, \tag{1}$$

where ω is the angular frequency of the wave in the inertial frame in which we work, m is the azimuthal wave number such that the wave varies with azimuthal angle φ as $e^{-im\varphi}$, ω_d is the particle azimuthal drift frequency due both to the bulk flow of the plasma in the inertial frame (the $E \times B$ drift) and to grad-B and curvature drifts (eastward for ions at Saturn), ω_b is the particle bounce frequency along the field lines, and N is any integer, positive, negative, or zero. However, net interchange of energy between waves and particles during the wave cycle requires that N be zero or even for waves whose magnetic fields are anti-symmetric about the equator ("odd" modes), such that the wave electric fields associated with the field line motion are symmetric, and that N be odd for waves whose magnetic fields are symmetric about the equator ("even" modes), such that the wave electric fields are antisymmetric [e.g., *Southwood and Kivelson*, 1982]. As indicated above, our observations suggest the latter condition pertains to the dawn patches, such that we focus here upon $N=\pm1$ drift-bounce resonance with symmetric (e.g., second harmonic) "even" magnetic modes, rather than $N = 0$ drift resonance with antisymmetric (e.g., fundamental) "odd" magnetic modes.

[33] We start by considering the wave parameters in equation (1) suggested by our observations. First, the azimuthal wave number m, equal to the total number of wavelengths in azimuth around the planet, can be found from the LT separation of successive auroral patches in the ionosphere, corresponding to one wavelength, or equivalently from the separation of patches in opposite hemispheres, corresponding to half a wavelength. From the histogram in Figure 5c it can be seen that the typical value of the latter is ~ 0.6 h LT, thus implying typically that $m \approx 20$. Corresponding ULF waves in the Earth's magnetosphere are also found to be of high m number, typically $m \approx 20 - 50$ [e.g., *Wright et al.*, 2001; *Baddeley et al.*, 2002, 2005]. Second, the angular frequency of the waves in the inertial frame ω can be found from the eastward angular velocity Ω of the auroral patches, the latter corresponding to the angular velocity of the wave phase fronts in the inertial frame. The angular frequency is then given by

$$\omega = m \ \Omega. \tag{2}$$

[34] From Figure 6 we find a typical value of $\Omega \approx 1.3 \times 10^{-4}$ $rad \ s^{-1}$ corresponding to a patch rotation period of ~14 h, which with $m \approx 20$ gives $\omega \approx 2.6 \times 10^{-3} \ rad \ s^{-1}$, corresponding to an oscillation period in the inertial frame of ~40 min. We note that *Kleindienst et al.* [2009] have shown that packets of Alfvénic field fluctuations at such frequencies (the above corresponding to ~0.4 mHz) are indeed commonly observed with significant amplitudes in Saturn's equatorial outer magnetosphere (see, e.g., their Figures 1 and 2). However, they have not been extensively studied to date.

[35] Turning now to the particle frequencies, the drift frequency ω_d is the sum of those due to plasma rotation at angular velocity Ω_p (due to $E \times B$ drift) and to the bounce-averaged sum of the grad-B and curvature drifts associated with magnetic field inhomogeneity at angular frequency $\omega_{\Delta B}$. We note that the resonance condition given by equation (1) can then be written as $(\omega' - m\omega_{\Delta B}) = N\omega_b$, where $\omega' = m(\Omega - \Omega_p)$ is the angular frequency of the waves in the plasma rest frame. From the discussion of Figure 6 in section 3.2, the results of *Thomsen et al.* [2010] and *Arridge et al.* [2011] suggest typical plasma angular velocities of $\Omega_p \approx 0.7 \times 10^{-4} \ rad \ s^{-1}$ in the outer magnetosphere, corresponding to plasma rotation periods of ~25 h. The oscillation frequency in the plasma rest frame is then typically $\omega' \approx 1.3 \times 10^{-3} \ rad \ s^{-1}$, corresponding to a period of ~80 min. We also assume a dipole field approximation as a first estimate of the bounce-averaged magnetic inhomogeneity drift, such that

$$\omega_{\Delta B} \simeq \frac{f_{\Delta B}(\alpha_{eq})LW}{qB_{eq}R_S^2}, \tag{3}$$

where L is the equatorial radius of the field lines in planetary radii ($R_S = 60,268$ km as indicated above), W is the particle kinetic energy, q is the particle charge (where we assume singly-charged ions with $q = e$, the elementary charge), $B_{eq} = 21,136 \ nT$ is the dipole field strength at the planet's equator [*Burton et al.*, 2010], and $f_{\Delta B}(\alpha_{eq})$ is a slowly varying function of equatorial pitch angle α_{eq} with values between 2 and 3 for α_{eq} between 0° and 90°. We note that $N = \pm1$ drift-bounce resonance in a symmetric magnetic wave field favors smaller pitch-angle particles that spend significant time away from the node in the antisymmetric wave electric field at the equator. The particle bounce frequency in the dipole field approximation is similarly

$$\omega_b \simeq \frac{\pi}{f_b(\alpha_{eq})LR_S} \left(\frac{W}{2m}\right)^{1/2}, \tag{4}$$

where m is the particle mass, and $f_b(\alpha_{eq})$ is another slowly-varying function of equatorial pitch angle with values between 1.38 and 0.74 for α_{eq} between 0° and 90°. We note that functions $f_{\Delta B}(\alpha_{eq})$ and $f_b(\alpha_{eq})$ are defined by integrals over the particle bounce motion that must in general be evaluated numerically [*Hamlin et al.*, 1961], and such values have been employed in the results shown here (values are given in the caption to Figure 12). For most purposes, however, the simple approximate forms $f_{\Delta B}(\alpha_{eq}) \approx 2.1 + 0.9 \sin \alpha_{eq}$ and $f_b(\alpha_{eq}) \approx 1.3 - 0.56 \sin \alpha_{eq}$ are sufficient [e.g., *Baddeley et al.*, 2005].

[36] Results are shown in Figure 12, where the solid lines show the left side of equation (1) plotted versus ion energy W on a log-scale, where the purple, red, green, and blue lines correspond to equatorial pitch angles α_{eq} of 0°, 30°, 60°, and 90°, respectively. The similarly color-coded dashed lines correspond to the right side of equation (1), for $N = +1$ in the upper half of the plot and $N = -1$ in the lower half as indicated. Drift-bounce resonance for given N then occurs where the solid and dashed lines for a given pitch angle cross each other. For the case of protons in Figure 12a, drift-bounce resonance with $N = +1$ occurs at energies of a few keV, e.g., at ~5 keV for 30° smaller pitch angle particles, corresponding to the high-energy tail of the low-energy proton population in the outer magnetosphere with typical energies ~100 eV [*McAndrews et al.*, 2009], while drift-bounce resonance with $N = -1$ occurs at energies of a few MeV (off the scale of the plot), corresponding to the high-energy tail of the hot proton population with typical energies ~10 keV [*Dialynas et al.*, 2009]. Neither
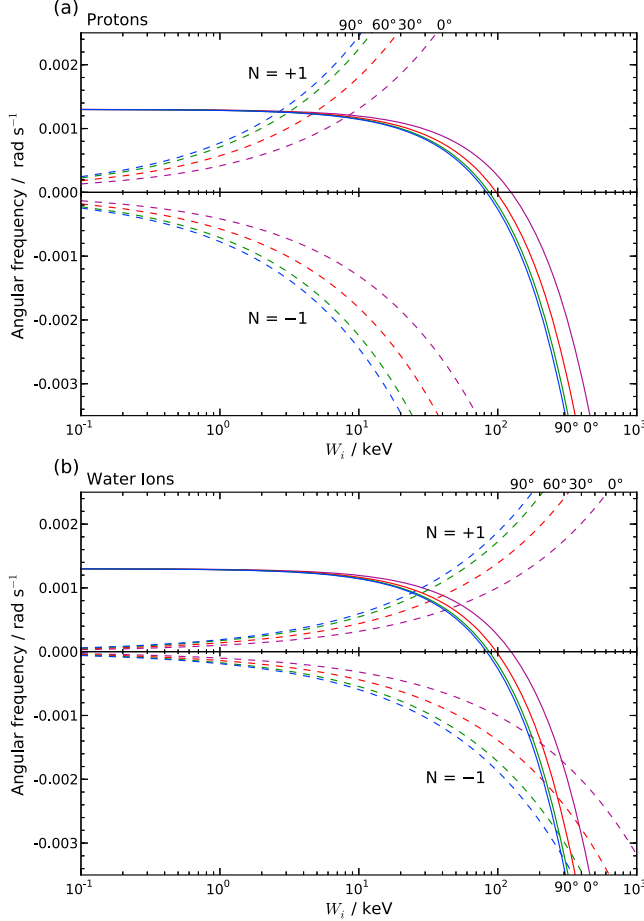
Figure 12. Plots showing conditions for drift-bounce resonance with ULF waves corresponding to the eastward-drifting dawn auroral patches, for (a) protons, and (b) water group ions (mass 17 assumed). The waves have azimuthal wave number $m = 20$, an oscillation frequency in the plasma rest frame of $\omega' = 1.3 \times 10^{-3} \ rad \ s^{-1}$, and are taken to have symmetric (e.g., second harmonic) magnetic perturbations relative to the equator so that principal resonances are those with $N = \pm 1$. In each panel the solid lines show the left side of equation (1) plotted versus ion energy W on a log scale, where purple, red, green, and blue correspond to equatorial pitch angles α_{eq} of $0°$, $30°$, $60°$, and $90°$, respectively (these curves being independent of ion mass). The similarly color-coded dashed lines correspond to the right side of equation (1), for $N = +1$ in the upper half of the plot and $N = -1$ in the lower half as indicated. Numerically-integrated values of the pitch-angle functions employed for $\alpha_{eq} = 0°$, $30°$, $60°$, and $90°$ are $f_{AB}(\alpha_{eq}) = 2.000, 2.552, 2.871,$ and 3.000, and $f_b(\alpha_{eq}) = 1.380, 1.000, 0.806,$ and 0.741, to three decimal places. Drift-bounce resonance occurs at ion energies where the solid and dashed lines of a given color cross. Drift resonance with $N = 0$ also occurs where the solid lines pass through zero near ~100 keV independent of ion mass, but the wave-particle energy exchange is zero for such particles for waves having symmetric magnetic and anti-symmetric electric perturbations.

condition thus corresponds to the central energy of a major proton population in Saturn's magnetosphere. For the case of water group ions in Figure 12b (mass 17 assumed), drift-bounce resonance with $N = +1$ occurs at energies of a few tens of keV, e.g., at ~30 keV for smaller $30°$ pitch angle particles, corresponding to typical energies of the hot water ion population in the outer magnetosphere, while drift-bounce resonance with $N = -1$ occurs at energies of a few hundred keV, corresponding to the high-energy tail of this population [*Dialynas et al.*, 2009]. The former condition is thus well placed to tap the energy of the main hot water ion population in the outer magnetosphere if the particle distribution function contains free energy in the form of nonmonotonic features.

[37] With regard to the disappearance of the auroral patches near to noon, we note that modeling of FLRs in the terrestrial context shows that they are strongly damped in the presence of auroral electron acceleration in the upward field-aligned current regions associated with their iono-spheric coupling [*Damiano and Johnson*, 2012], such as we infer to be present at Saturn. This suggests that the disappearance of the auroral patches near to noon may be related to the diminution of the "free energy" source within the driving hot ion population, followed by rapid damping of the waves. The hot ions are likely injected near to midnight and drift eastward via dawn, in conformity with the LT properties of the patches.

5.3. Properties of Second Harmonic Field Line Resonances

[38] Having shown that the hot water ion population forms a suitable drift-bounce resonant energy source in the outer magnetosphere, we now outline the nature of the ULF waves proposed to be excited, namely an even mode FLR, specifically the second harmonic. To illustrate the properties of such waves we employ the simple box model of *Wright and Allan* [1996], following *Southwood and Hughes* [1983], in which Cartesian x, y, and z coordinates represent the radial, azimuthal, and northward directions in the magnetosphere, respectively. In the unperturbed system the plasma is at rest (i.e., we work in the frame of the large-scale flow), the magnetic field is uniform in the z direction, taken here to be given by $\boldsymbol{B} = -B\,\hat{\boldsymbol{z}}$ to represent the north-to-south field of Saturn, and the plasma density ρ varies in the x direction, taken here to fall with x so that the Alfvén speed rises. The system is then limited in the z direction by two plane boundaries of large but finite Pedersen conductivity Σ_P, representing the two ionospheres, located at $z = \pm l$, such that $z = 0$ represents the equator.

[39] The waves in this system are characterized by three scale lengths or wave numbers, corresponding to the three spatial coordinates, namely δ_x, k_y, and k_z. The wave numbers are k_y in the y (azimuthal) direction, such that the wave varies as $\exp j(k_y y - \omega t)$, and k_z in the z (northward) direction, to lowest order quantized by the ionospheric boundary conditions according to

$$k_z = \frac{n\pi}{2l}, \tag{5}$$

for n any positive integer. When n is odd, as studied by *Wright and Allan* [1996], the transverse magnetic and electric perturbations vary as $\sin(k_z z)$ and $\cos(k_z z)$, respectively, thus being antisymmetric and symmetric about the equator,
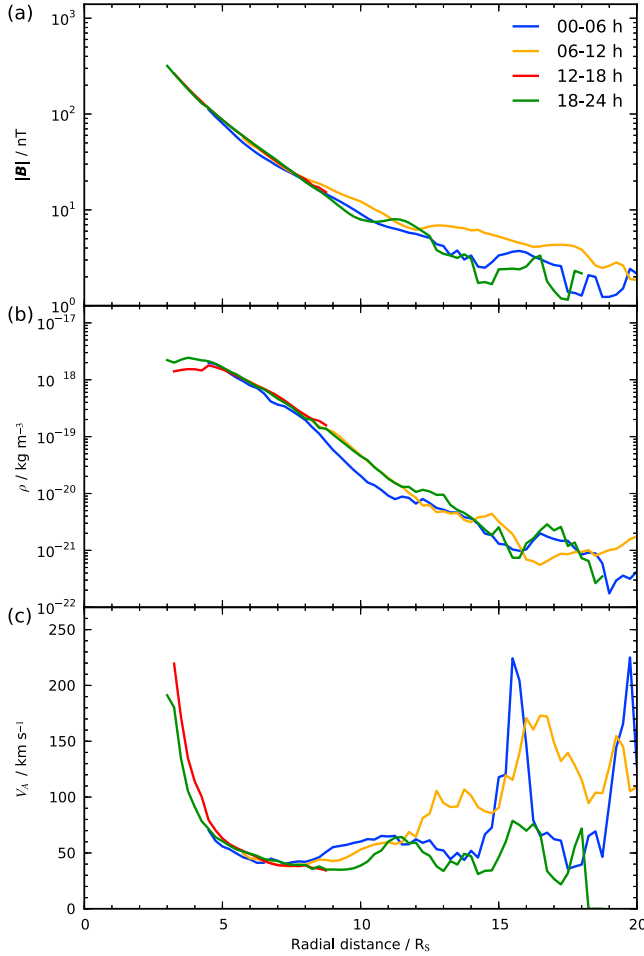
Figure 13. Plots showing radial profiles in Saturn's equatorial plane of (a) the magnetic field strength, (b) the plasma mass density, and (c) the Alfvén speed. The field and plasma parameters were derived by *Kellett et al.* [2011] from eleven orbits of closely equatorial Cassini data, these data being divided into four color-coded LT quadrants as indicated in the figure.

as indicated above. However, when n is even, as studied here, the transverse magnetic and electric perturbations vary as $\cos(k_z z)$ and $\sin(k_z z)$, respectively, thus being symmetric and antisymmetric about the equator. In both cases, to lowest order, the ionospheres form nodes in the wave electric field (and plasma flow), and antinodes in the transverse magnetic field. The corresponding angular frequency ω of the wave for a mode n field line resonance at position $x = x_R$ is given by

$$\omega = k_z \, V_A(x_R) = \frac{n\pi}{2l} V_A(x_R), \tag{6}$$

where $V_A(x) = B/\sqrt{\mu_o \rho(x)}$ is the Alfvén speed. The spatial scale δ_x of the resonant region in the x direction about x_R is then given for any n by

$$\delta_x = \left(\frac{2}{n\pi}\right) \frac{1}{\mu_o \Sigma_P (dV_A/dx)_{x=x_R}}. \tag{7}$$

[40] This equation may be obtained from equation (18) of *Wright and Allan* [1996], with the use of their equations (15) and (16) and the above expression for the Alfvén speed V_A (x) (see also the Appendix).

[41] We now apply this model to the dawn patch observations presented in section 3, assuming that this phenomenon corresponds to a resonance of the required north-south symmetry, $n = 2$, propagating eastward in the outer magnetosphere. First, the wave number k_y in the y direction should correspond to azimuthal wave number $m \approx 20$ at a radial distance of ~20 R_S, thus implying an east-west wavelength $\lambda_y \approx 2\pi \simeq 6 \, R_S$ such that $k_y \approx 1 \, R_S^{-1}$. Second, equation (5) gives $k_z l \approx \pi$ with $n = 2$, where l is the effective length of the field lines from the equator to the Pedersen-conducting ionospheric boundary. Unlike the box model, however, the Alfvén speed V_A varies strongly along field lines in Saturn's magnetosphere, with equation (6) being generalized to

$$\omega \approx \frac{n\pi}{\displaystyle\int_{-L}^{L} \frac{ds}{V_A(s)}}, \tag{8}$$

where s is distance along field lines of total length $2L$. Consideration of equation (8) shows that length l corresponds essentially to the half-width of the central plasma layer where the density remains high due to equatorial confinement of the rotating plasma and the field strength remains low, such that the Alfvén speed is also low, thus making the dominant contribution to the propagation time integral. Plasma observations indicate that $l \approx 5 \, R_S$ is reasonable in the outer magnetosphere [*Richardson*, 1995; *Thomsen et al.*, 2010], such that $\lambda_z \approx 10 \, R_S$ for $n = 2$ and $k_z \approx \pi/5 \simeq 0.6 \, R_S^{-1}$. Third, we check the consistency of equation (6) with our above estimate of the wave angular frequency in the plasma rest frame, $\omega' \approx 1.3 \times 10^{-3} \, rad \, s^{-1}$, such that we need to know the value of the equatorial Alfvén speed. This is shown in Figure 13, where in Figures 13a and 13b we show radial profiles spanning ~3 to ~20 R_S of the equatorial magnetic field strength and plasma mass density, respectively, determined by *Kellett et al.* [2011] from eleven orbits of the Cassini spacecraft, together with the consequent Alfvén speed in Figure 13c. The data have been divided into four color-coded LT sectors as indicated in the figure, plotted over the radial ranges for which data exists, of which the 6–12 h LT data (yellow lines) is most germane here. It can be seen that the Alfvén speed falls rapidly with distance in the inner magnetosphere, before flattening and then rising again with much variability in the outer dayside region, where $V_A \approx 100 \, km \, s^{-1}$. Substitution of this value into equation (6) with $n = 2$ and $l \approx 5 \, R_S$ then yields a frequency $\omega \approx 1.0 \times 10^{-3} \, rad \, s^{-1}$, in excellent consistency with the value $\omega' \approx 1.3 \times 10^{-3} \, rad \, s^{-1}$ deduced from observations. Fourth, the radial scale of the resonance δ_x is not obviously determinable from equation (7), because although we may estimate $\Sigma_P \approx 8 \, mho$ in the morning auroral zone from the work of *Galand et al.* [2011], Figure 13 suggests that a wide range of spatial scales may be present in the outer region. Here we simply assume sufficiently steep spatial gradients in the Alfvén speed, comparable to the largest suggested in the figure, such that the resonant region is sharply defined. Specifically, we take for definiteness $\delta_x \approx 0.3 \, R_S$, with the main current region then extending radially over ~1 R_S in the equatorial plane (see below). This range maps to approximately half a degree of latitude in the ionosphere (~500 km north-south), rather less than is indicated by the projected images in Figures 2 and 7. However, as indicated in section 2, the latter are significantly broadened by the projection of obliquely viewed emission, which also has a finite vertical extent in the atmosphere.
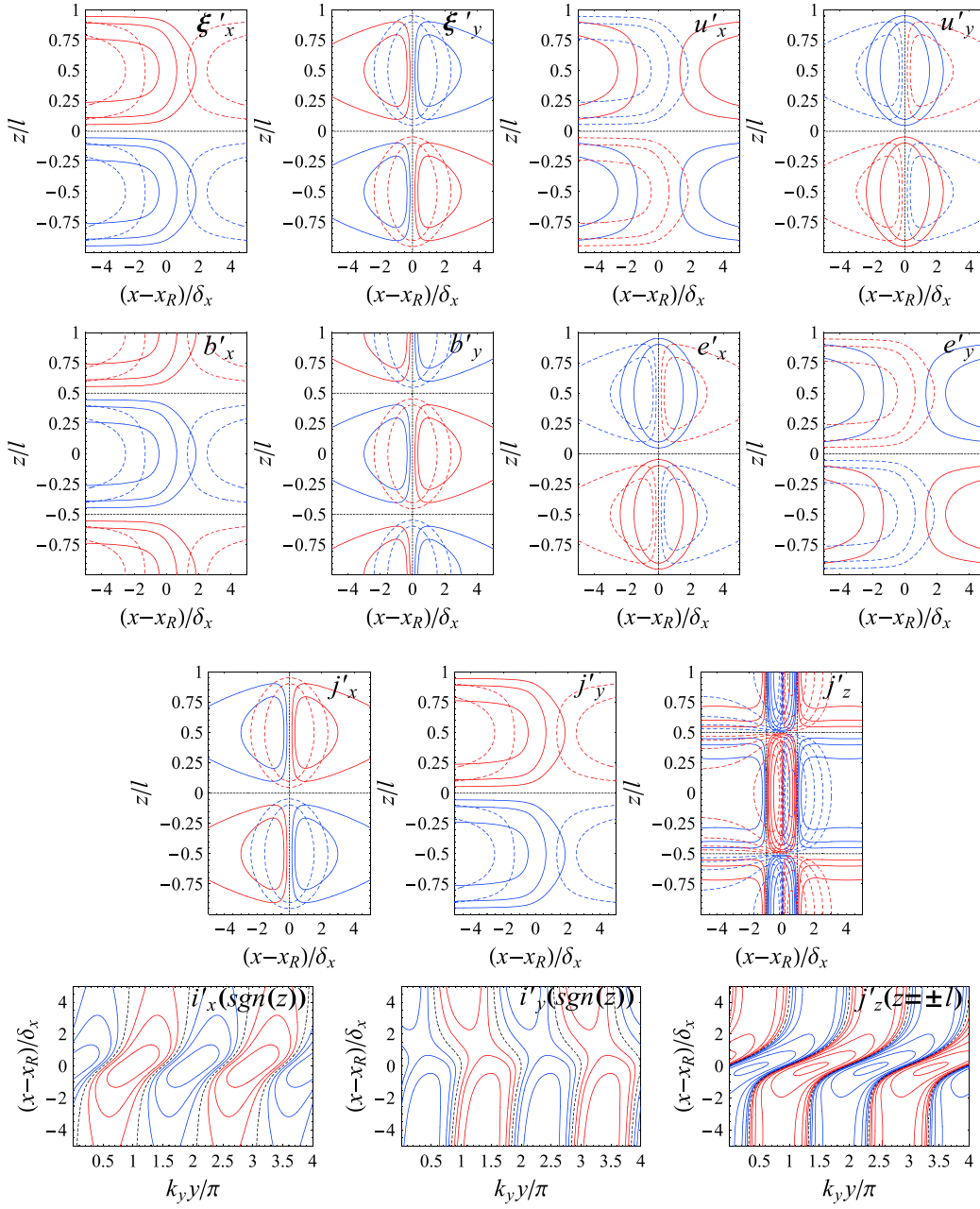
Figure 14. Montage of plots illustrating the properties of a second harmonic ($n=2$) Alfvén resonance obtained from the *Wright and Allan* [1996] box model (see Appendix), specifically for model parameters $k_y \delta_x = 0.3$, and $k_y l = 5$. The top three rows of plots show contours of normalized parameters plotted in the $x - z$ plane, while the bottom row similarly shows contours in the $x - y$ plane at the two ionospheric boundaries ($z/l) = \pm 1$. The x coordinate represents the radial direction in the equatorial region and the poleward direction in both hemispheres, y represents the azimuthal direction positive eastward, and z is antiparallel to the background field, northward in the equatorial region. The x coordinate is normalized to δ_x and shown relative to the position of the resonant field line at $x = x_R$, y to π/k_y, and z to the effective half-length of the field lines l. Zero contours are indicated by black dotted lines, while red and blue contours show positive and negative normalized values, respectively, differing by factors of 2 from each other, starting with lowest values of ± 0.5 nearest the zero lines. In the $x - z$ plots, the dashed and solid contours correspond to $k_y y/\pi = 0$, 2, 4 …. and $k_y y/\pi = 0.5$, 2.5, 4.5 …., respectively. Values for the other half wave cycle may be obtained simply by interchanging red and blue. The top row shows the normalized field line displacements in the x and y directions $\xi'_{x,y}$ and velocities $u'_{x,y}$, the second row the normalized magnetic and electric fields $b'_{x,y}$ and $e'_{x,y}$, and the third row the normalized current densities $j'_{x,y,z}$. The $x - y$ plots in the bottom row show the height-integrated Pedersen currents $i'_{x,y}$ in the northern ionosphere, the sign of which reverses in the southern hemisphere, together with the ionospheric field-aligned current density j'_z applicable to both hemispheres by virtue of the symmetry. The plots correspond specifically to time $t=0$ and arbitrary phase $\phi=0$ in the formulas in the Appendix, with the perturbations then propagating in the y direction with phase speed ω/k_y, with ω given by equation (6).

[42] In Figure 14 we show a montage of wave parameter plots obtained from the *Wright and Allan* [1996] box model, the formulas for which are given in the Appendix, illustrating the nature of the magnetosphere-ionosphere perturbations considered here. Following the above discussion, the model parameters employed are $n = 2$ (second harmonic), $k_y \delta_x = 0.3$, and $k_y l = 5$. The top three rows of plots show contours of normalized parameters plotted in the $x - z$ plane, recalling that x represents the radial direction, and z northward antiparallel to the background field. The x coordinate is normalized to δ_x given by equation (7) and shown relative to the resonant field line for angular frequency ω at $x = x_R$ over the range ± 5 (representing a physical length at the equator of ~ 3 R_S), while z is normalized to the effective half-length of the field lines l (a physical length of ~ 5 R_S), such that the highly conducting model boundaries are located at the top and bottom of the plot at ± 1. The y coordinate representing the azimuthal direction, positive eastward, is then directed into the plane of these diagrams, normalized to π/k_y (a physical length of ~ 3 R_S). Zero values are indicated by black dotted lines, while red and blue contours show positive and negative normalized values, respectively, which differ by factors of 2 from each other, starting with lowest values of ± 0.5 nearest the zero lines. Dashed and solid contour lines correspond to $k_y y/\pi = 0$, 2, 4 .... and $k_y y/\pi = 0.5$, 2.5, 4.5 ...., respectively, with values for the other half wave cycle being obtained simply by interchanging red and blue. The plots correspond specifically to time $t = 0$ in the formulas in the Appendix (and arbitrary phase $\phi = 0$), with the perturbation then propagating in the y direction with time at phase speed ω/k_y.

[43] The top row of plots in Figure 14 show the normalized field line displacements in the x and y directions $\xi'_{x,y}$ and velocities $u'_{x,y}$, the second row the normalized magnetic and electric fields $b'_{x,y}$ and $e'_{x,y}$, and the third row the normalized current densities $j'_{x,y,z}$. As discussed above, the magnetic perturbations are symmetric about the equator, with nodes at $(z/l) = \pm 0.5$, and antinodes at the equator and at the boundaries $(z/l) = \pm 1$. Conversely, the electric field, together with the plasma velocities, field displacements, and transverse currents, are antisymmetric about the equator, with antinodes at $(z/l) = \pm 0.5$, and nodes at the equator and at the boundaries. The field-aligned current j'_z, however, is again symmetrical about the equator, with nodes at $(z/l) = \pm 0.5$, and antinodes at the equator and at the boundaries. This symmetry means, however, that the field-aligned current is oppositely directed relative to the ionosphere at conjugate points in the two hemispheres, such that if the current is into the ionosphere in one hemisphere, it is out of the ionosphere in the other, and vice versa.

[44] The ionospheric currents themselves are shown in the bottom row of Figure 14, where we plot contours of normalized parameters in the $x - y$ plane at the two ionospheric boundaries $(z/l) = \pm 1$, where in the ionosphere positive x represents the poleward direction in both hemispheres, and y is again positive eastward. Specifically, we show contours of the field-aligned current j'_z applicable to both hemispheres by virtue of the symmetry, together with the height-integrated Pedersen currents $i'_{x,y}$ which close this current specifically for the northern ionosphere. The sign of the latter currents is reversed in the southern hemisphere. It can

be seen that strong oscillatory peaks in the upward and downward field-aligned current occur within a few δ_x of the resonance, as indicated above. Upward currents, potentially associated with downward electron acceleration and auroras, correspond to blue regions in the northern hemisphere and red regions in the southern, thus displaying the symmetry properties observed in the dawn auroral patches. For the parameters chosen, the main upward current regions have a north-south physical dimension of ~ 500 km in the ionosphere, with successive regions of given sign being displaced ~ 5000 km east-west in a given hemisphere.

6. Physical Origin of Dusk Transients

[45] The exclusively nonconjugate nature of the dusk transient events demonstrated in section 4 shows that they cannot be produced by processes on closed field lines such as magnetospheric hot plasma injections or ULF waves that would inevitably result in simultaneous emission from both hemispheres. Instead, our results suggest that open field lines may be involved for which conjugacy is not mandatory, which we therefore consider here. Specifically, we discuss emissions associated with bursts of magnetic reconnection at the dayside magnetopause, and consider their location, conjugacy, and lifetime.

[46] With regard to the postnoon location of the events, we note that magnetic reconnection is expected to be suppressed by strong velocity shear across the boundary, when the shear parallel to the reconnecting fields becomes comparable with the Alfvén speed [*Owen and Cowley*, 1987; *La Belle-Hamer et al.*, 1995; *Cassak and Otto*, 2011]. As discussed previously for the case of Jupiter by *Desroche et al.* [2012], the subsolar and dusk side of the magnetopause at Saturn is thus favored for large-scale reconnection compared with dawn due to the asymmetry imposed by the interior rotation flow. The plasma angular velocity in the outer magnetosphere envisaged in section 3.2 corresponds to an eastward flow of ~ 100 km s^{-1} adjacent to the boundary as previously indicated in section 5.1, which is likely to be matched in the postnoon magnetosheath near ~ 14 h LT for the low solar wind flow conditions pertaining here (Figure 1), thus reducing the flow shear across the boundary to minimum values in this sector. A link between reconnection events and transient emissions with a mean location of formation at ~ 14.5 h LT as shown in Figure 9 (section 4.2), thus seems plausible.

[47] We then consider the effects associated with a burst of reconnection at the postnoon magnetopause, such that patches of new open flux are formed in the ionosphere lying initially just equatorward of the preexisting open-closed field boundary. Although magnetosheath plasma will then precipitate into the atmosphere in these patches in both hemispheres, containing equal amounts of newly opened magnetic flux, the associated energy flux is entirely insufficient to produce bright detectable UV auroras [e.g., *Cowley et al.*, 2004].

[48] Instead, we need to consider the field-aligned currents associated with velocity perturbations on the open flux tubes, the north-south symmetry of which is broken by the presence of the east-west (Y) component of the interplanetary magnetic field (IMF). This is sketched in Figure 15, where Figures 15a and 15b show the situation for positive and negative IMF B_y (and positive B_z), respectively. The sketches on the left of these panels show newly opened field lines in the postnoon sector in each case, in views looking from the
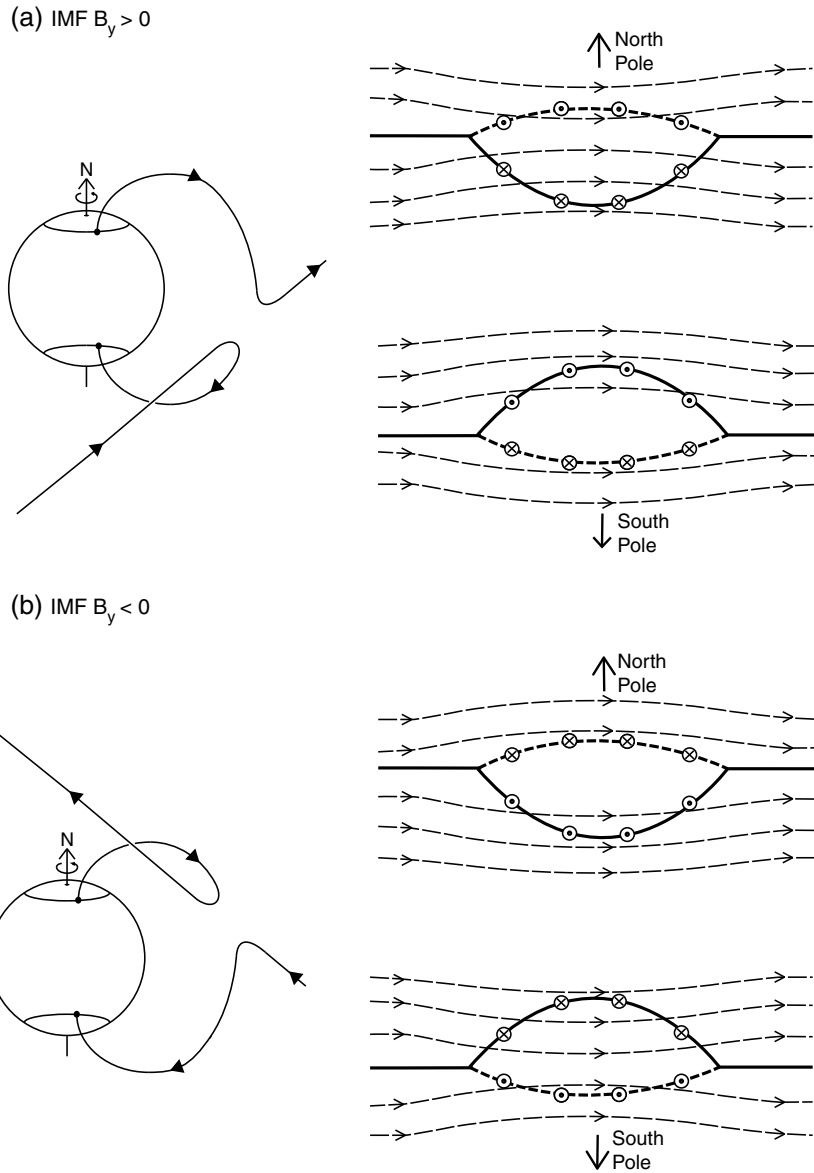
Figure 15. Sketches illustrating the north-south asymmetries on newly opened flux tubes due to the presence of IMF B_y, where it shows the cases of (a) positive and (b) negative IMF B_y (and positive B_z). The sketches on the left in each panel show newly-opened field lines in the postnoon sector in each case, in views looking from the direction of the Sun, showing the senses of the field tension force associated with the east-west field. For near-antiparallel reconnection, the reconnection site is displaced into the southern hemisphere for positive B_y and into the northern hemisphere for negative B_y, as shown. The effects on the plasma flow and currents in the northern and southern ionospheres are sketched in the upper and lower diagrams on the right in each panel, respectively. The solid lines show the open-closed boundary in each hemisphere, displaced equatorward in the central region by the reconnection event forming the equatorward limit of the patches of new open flux, while the short-dashed lines show the former boundary marking the poleward limit of the patches, perturbed poleward as they transfer into the polar cap. The arrowed long-dashed lines show plasma streamlines, while the circled dots and crosses show the regions of upward and downward field-aligned currents, respectively, on the boundary of the open patch.

direction of the Sun. It can be seen for B_y positive that the effect of the field tension on the newly opened flux tubes enhances the duskward flow of the field lines in the north, while retarding it in the south, and vice versa for B_y negative. In addition, if reconnection between near-antiparallel fields is favored, as suggested in relation to plasma β effects at the boundary by *Masters et al.* [2012b] and *Desroche et al.* [2012], then the reconnection sites may be displaced away from the equator, into the southern hemisphere for B_y positive and into the northern hemisphere for B_y negative, as shown in the sketches. If so, the retardation effect in one hemisphere may be more effective than the enhancement in the other, because in both cases the former involves the "short" branch of the newly open field lines and the latter the "long." The "short" branch implies more

prompt and effective communication with the ionosphere via Alfvén waves than the "long" branch, due to the shorter propagation path with higher wave speeds away from the central plasma sheet. Simple estimates suggest one-way communication times of ~15 min in former case, and ~1 h in the latter.

[49] The effects on the plasma flow and currents in the northern and southern ionospheres are sketched in the upper and lower diagrams on the right of each panel in Figure 15, respectively, where the arrowed long-dashed lines show plasma streamlines, and the patch of new open flux in each hemisphere is contained between the equatorward-displaced open-closed boundary on the equatorward side (solid line), and the perturbed former open-closed boundary on the poleward side (short dashed lines). We have assumed, for simplicity, similar significantly sub-corotating flows on both open and closed field lines in the unperturbed state, such that an approximately uniform ionospheric Pedersen current flows equatorward across the boundary in both hemispheres. This simple initial state allows us to focus on the essential asymmetry associated with the newly opened flux tubes.

[50] Considering first the effects for IMF B_y positive in Figure 15a, it can be seen that the enhancement of the duskward plasma flow on newly opened flux tubes in the northern hemisphere reduces the equatorward current within the patch, hence requiring upward field-aligned currents to flow on its poleward side, indicated by circled dots, and equal and opposite downward currents to flow on its equatorward side, indicated by circled crosses. Simultaneously, reduction of the duskward flow on the newly opened flux tubes in the southern hemisphere enhances the equatorward current within the patch, requiring downward currents to flow on its poleward boundary and equal upward currents to flow on its equatorward boundary. Consideration of auroral emissions then focuses on the regions of upward current, which for IMF B_y positive in Figure 15a will be carried by cool, dense magnetosheath plasma at the poleward boundary of the patch in the northern hemisphere, generally not requiring strong field-aligned acceleration of the electrons, but at least partially by hot tenuous magnetospheric plasma at the equatorward boundary of the patch in the southern hemisphere, the latter then requiring strong field-aligned electron acceleration leading to bright auroras [e.g., *Cowley et al.*, 2004]. For IMF B_y positive, therefore, we may expect transient bright auroras to be associated with patches of newly-opened flux tubes in the south, but not in the north. For IMF B_y negative shown in Figure 15b, however, the sense of the current asymmetry is reversed, leading to the expectation of bright auroras at the equatorward boundary of the patch in the north, but not at the poleward boundary in the south by the same argument. We note that in both cases the bright auroras are expected to occur in the hemisphere where the eastward motion of the new open field lines is retarded by the field tension, an effect that may be enhanced by off-equatorial near-antiparallel reconnection as noted above. Although simplistic, this discussion nevertheless illustrates how magnetopause reconnection events can lead to postnoon nonconjugate transient emissions that occur in only one hemisphere, but with roughly equal numbers of such events occurring in the northern and southern hemispheres depending on IMF B_y.

[51] With regard to the lifetime of the transient auroral events, we note that in the above scenario this relates to the time scale for relaxation of the field tension effect leading to retarded flows in one hemisphere. Such relaxation will occur as the magnetosheath plasma adjacent to the magnetopause accelerates in the tailward flow back toward speeds comparable to those in the upstream solar wind, considerably in excess of speeds in the outer magnetosphere, leading to a reversal in sense of the flow perturbation from retardation to enhancement, as in the opposite hemisphere. The retardation effect is therefore transient, with corresponding transient auroras occurring in the interval in which the associated field-aligned currents remain sufficiently strong to generate bright emissions. The flow perturbations in the magnetosheath associated with the field tension will be of order the Alfvén speed, ~50 km s^{-1}, thus producing a significant effect corresponding to roughly half the speed of the transverse flow near the reconnection site, while the time required for the magnetosheath flow to accelerate by a comparable amount downstream of the reconnection site is estimated from simple models to be ~30–40 min (equivalent to 2–3 one-way Alfvén transit times between the magnetopause and ionosphere on the "short" open field branch). The transient auroral lifetimes of ~10–30 min in Figure 10 then correspond roughly to a half of this interval, which appears not unreasonable. We note that in the interval of ~30–40 min following postnoon reconnection, the open tubes will have propagated only ~5 R_S around the magnetopause toward dusk, corresponding to ~1 h of LT. The expected overall eastward motion of the transient aurora over their lifetime is thus small, such that the scattered nature of the angular velocity measurements in Figure 11 is perhaps not surprising. The estimated overall time scale for propagation to the night side via dusk in the accelerating flow is ~100 min.

[52] We briefly note here that a possible alternative scenario for strictly nonconjugate dayside emissions that is perhaps worth future consideration involves high-latitude lobe reconnection, one hemisphere at a time, during intervals of southward IMF. However, given a largely tailward magnetosheath flow adjacent to the high-latitude lobe magnetopause, the origin of the strong preference for transient emissions in the dusk sector may then be less obvious.

[53] The above discussion clearly prompts consideration of the hemispheric occurrence of these dusk transient events in relation to the IMF vector upstream of the magnetosphere, particularly with regard to the Y component that governs the hemispheric asymmetries as outlined above, as well as the Z component that also regulates the location and rate of reconnection. We note, however, that the correlation study presented by *Zieger and Hansen* [2008] between observed and modeled interplanetary parameters shows that the IMF Y component is only moderately well predicted, while the Z component cannot be predicted at all. It is thus perhaps unsurprising that examination reveals no clear correspondence between the northern and southern transient events found here and the modeled Y component corresponding to the propagated parameters in Figure 1.

7. Summary

[54] In this paper we have examined Saturn's dayside UV auroral emissions using HST ACS/SBC image data obtained on 32 near-opposition visits close to Saturn equinox in January–March 2009, when the Saturn sub-Earth latitude was only ~2°. Auroral emissions from both northern and southern

hemispheres could thus be simultaneously, if somewhat obliquely, observed, allowing issues of interhemispheric conjugacy uniquely to be investigated. Previous studies of Saturn's dayside emissions have established the existence of two types of small-scale features, namely relatively long-lived eastward-drifting patches in the dawn-to-noon sector discussed previously by *Grodent et al.* [2011], and ~10–30 min transient emissions in the dusk sector discussed previously by *Radioti et al.* [2009]. Here we have further examined related phenomena, focusing on issues of interhemispheric conjugacy, and implications for physical origins. The near-equinox interval investigated also corresponded to conditions of extreme solar quiet at the minimum of the solar cycle, with MHD-model predicted solar wind dynamic pressures that are moderate to low, such that the subsolar radius of Saturn's magnetosphere is expected typically to lie in the range ~20–30 R_S, sometimes expanding as far as ~ 40 R_S.

[55] The equinox campaign images show that eastward-propagating patches are commonly present in the dawn-to-noon sector, being observed on ~70% of all HST visits. When they are observed, they are nearly always observed in both northern and southern hemispheres during a visit. Unexpectedly, however, the emission maxima are found generally not to be conjugate north and south, but are instead typically displaced in LT by ~0.5–1 h. When multiple patches are present, maxima in one hemisphere typically fall near minima in the other. Angular velocities of rotation, while broadly spread, are found to average ~80% of rigid corotation, similar to typical ~70% values reported for auroral "spots" by *Grodent et al.* [2011]. These values are somewhat larger than the typical plasma angular velocities of ~40–50% of rigid corotation reported by *Thomsen et al.* [2010] and *Arridge et al.* [2011] for the outer magnetosphere to which these emissions are likely conjugate. Our results thus suggest that the patches propagate eastward through the plasma at modest relative angular speeds.

[56] These properties are consistent with those expected for a second harmonic ULF FLR wave propagating eastward through the plasma, for which the magnetic field and field-aligned current perturbations are symmetric about the equator, thus being consistent with the above conjugacy findings. In this interpretation the waves have azimuthal wave number $m \approx 20$, and propagate eastward with a wave period in the plasma rest frame of ~80 min, compared with ~40 min in the inertial frame. This period is consistent with expectations for a second harmonic resonance in the outer magnetosphere for an observed equatorial Alfvén speed of ~100 km s^{-1} and a plausible effective length of the field lines of ~10 R_S. With regard to the origin of the ULF wave, both symmetry and propagation properties have been shown to be inconsistent with a Kelvin-Helmholtz source excited in the magnetospheric boundary region. However, $N = +1$ drift-bounce resonance with water ions at energies of a few tens of keV is a plausible mechanism for wave generation, such ions forming a major component of the hot plasma population in Saturn's outer magnetosphere.

[57] The equinox data set shows that transient dusk emissions are also a common phenomenon, but not as common as dawn patches, being observed on ~40% of the HST visits of ~ 40 min total duration. These emissions are also found to be nonconjugate, but now in the more strict sense that transient enhancements in one hemisphere are entirely unaccompanied

by enhancements in the other. However, examples of such enhancements were observed in both the northern and southern hemispheres, those reported in pre-equinox HST data by *Radioti et al.* [2009] perforce being located exclusively in the south. Such extreme nonconjugate behavior suggests an association with open flux tubes for which approximate conjugacy is not mandatory, and we have discussed one scenario in which north-south symmetry is broken on newly-opened dayside flux tubes through the agency of the east-west (Y) component of the IMF, generally the major IMF component in the outer solar system. The picture proposed has been shown to be plausibly consistent with preferential event occurrence in the postnoon sector, equal overall numbers of events north and south, and time scales of a few tens of minutes, though the expected relationship with the sign of the IMF Y component remains to be established observationally. Further examination of conjugate auroral properties from Earth, however, will now have to await observations uring the next Saturn equinox, occurring in April 2024.

Appendix A: Formulae for Alfvén Resonance Box Model

[58] Here we outline the governing equations and resulting formulae for the *Wright and Allan* [1996] box model of Alfvén resonances employed to construct Figure 14, specifically focusing on the even modes applicable to this paper (noting that *Wright and Allan* [1996] focused specifically on, and gave formulas for, the odd modes). For examples of previous uses of this model in a terrestrial context see, e.g., *Milan et al.* [2001] and *Scoffield et al.* [2007].

[59] The box model employs three orthogonal right-handed Cartesian coordinates, x representing the radial direction at the equator and the poleward directions in both ionospheres, y the azimuthal direction positive eastward, and z the field-aligned coordinate northward at the equator. In the unperturbed system the magnetic field is taken to be uniform, $\boldsymbol{B} = \pm B\,\hat{\boldsymbol{z}}$ (where in Figure 14 we take the lower sign representing the southward field at Saturn), while the plasma is at rest, $\boldsymbol{U} = \boldsymbol{0}$, and of mass density $\rho = \rho(x)$. The system is terminated at $z = \pm\, l$ by boundaries of high but finite Pedersen conductivity Σ_P. Writing wave perturbations using lower case symbols and linearizing, the basic equations governing the system are Faraday's law and the momentum equation

$$\frac{\partial \boldsymbol{b}}{\partial t} = \mathrm{curl}(\boldsymbol{u} \times \boldsymbol{B}) \quad \text{and} \quad \rho \frac{\partial \boldsymbol{u}}{\partial t} = \boldsymbol{j} \times \boldsymbol{B} = \frac{1}{\mu_o}(\mathrm{curl}\,\boldsymbol{b}) \times \boldsymbol{B},$$

$$(\text{A1})$$

where the wave electric field is $\boldsymbol{e} = -\,\boldsymbol{u} \times \boldsymbol{B}$, $\boldsymbol{j}$ is the electric current density in the plasma, and the displacement current and plasma pressure have been neglected. We also have $\boldsymbol{u} = (\partial \boldsymbol{\xi}/\partial t)$ where $\boldsymbol{\xi}$ is the plasma and field line displacement from its unperturbed position, such that both the wave electric and magnetic fields (and hence current densities) can be written in terms of $\boldsymbol{\xi}$ and its derivatives ($\boldsymbol{b} = \mathrm{curl}(\xi \times \boldsymbol{B})$ from Faraday's law). We assume sinusoidal propagation in the y direction as $e^{i\Phi(y,t)}$ with $\Phi(y,t) = (k_y y - \omega t + \phi)$, where angular frequency ω corresponds to an Alfvén resonance of order n at $x = x_R$ (equation (6)), and ϕ is an arbitrary constant. Introducing normalized variable $X = (x - x_R)/\delta_x$ in the x direction (where δ_x is given by equation (7)), the lowest-order even

mode ($n = 2, 4, 6, \ldots.$) solutions for ξ_x and ξ_y in the vicinity of the resonance are given in complex form by

$$\xi_x = \xi_{xo} \sin\left(\frac{n\pi z}{2l}\right) G(X) e^{i\Phi(y,t)} \quad \text{and} \quad \xi_y = \frac{i}{k_y \delta_x} \frac{\partial \xi_x}{\partial X}, \quad \text{(A2)}$$

from which all other perturbed quantities follow (the height-integrated ionospheric Pedersen current intensities i at $(z/l) = \pm 1$ through $\boldsymbol{i} = \mp(\hat{z} \times \boldsymbol{b})/\mu_o$ from Ampère's law). Complex function $G(X) = G_r + iG_i = \ln(X - i)$ (see further below), and the physical quantities are taken to be the real parts of these expressions. We note that at this order the field-aligned components u_z and b_z are both zero. We also note that the expression for the odd modes ($n = 1, 3, 5, \ldots.$) simply replaces sin with cos in the z function in equation (A2).

[60] It is convenient to normalize displacements to ξ_{xo}, velocities to $\omega \xi_{xo}$, electric fields to $\omega \xi_{xo} B$, magnetic fields to $(n\pi/2l)\xi_{xo} B$, current densities to $(n\pi/2l)^2 \xi_{xo} B/\mu_o$, and ionospheric current intensities to $(n\pi/2l)\xi_{xo} B/\mu_o$. We then obtain the following normalized forms for the even modes with $n = 2, 4, 6, \ldots.$

$$\xi'_x = \sin\left(\frac{n\pi z}{2l}\right)(G_r \cos\Phi - G_i \sin\Phi)$$

$$\xi'_y = -\frac{1}{k_y \delta_x} \sin\left(\frac{n\pi z}{2l}\right)(F_r \cos\Phi - F_i \sin\Phi) \quad \text{(A3)}$$

$$u'_x = \sin\left(\frac{n\pi z}{2l}\right)(G_i \cos\Phi + G_r \sin\Phi)$$

$$u'_y = -\frac{1}{k_y \delta_x} \sin\left(\frac{n\pi z}{2l}\right)(F_i \cos\Phi + F_r \sin\Phi)$$

$$e'_x = \pm \frac{1}{k_y \delta_x} \sin\left(\frac{n\pi z}{2l}\right)(F_i \cos\Phi + F_r \sin\Phi)$$

$$e'_y = \pm \sin\left(\frac{n\pi z}{2l}\right)(G_i \cos\Phi + G_r \sin\Phi)$$

$$b'_x = \pm \cos\left(\frac{n\pi z}{2l}\right)(G_r \cos\Phi - G_i \sin\Phi)$$

$$b'_y = \mp \frac{1}{k_y \delta_x} \cos\left(\frac{n\pi z}{2l}\right)(F_r \cos\Phi - F_i \sin\Phi)$$

$$j'_x = \mp \frac{1}{k_y \delta_x} \sin\left(\frac{n\pi z}{2l}\right)(F_r \cos\Phi - F_i \sin\Phi)$$

$$j'_y = \mp \sin\left(\frac{n\pi z}{2l}\right)(G_r \cos\Phi - G_i \sin\Phi)$$

$$j'_z = \pm \left(\frac{2k_y l}{n\pi}\right) \cos\left(\frac{n\pi z}{2l}\right) \left(\left(\frac{H_r}{(k_y \delta_x)^2} + G_i\right) \cos\Phi\right.$$
$$\left. - \left(\frac{H_i}{(k_y \delta_x)^2} - G_r\right) \sin\Phi\right)$$

$$i'_x = \mp \frac{1}{k_y \delta_x} \cos\left(\frac{n\pi}{2}\right)(F_r \cos\Phi - F_i \sin\Phi)$$

$$i'_y = \mp \cos\left(\frac{n\pi}{2}\right)(G_r \cos\Phi - G_i \sin\Phi)$$

where the alternative signs refer specifically to the two choices $\boldsymbol{B} = \pm B \, \hat{z}$, and the expressions for the ionospheric

currents i'_x and i'_y refer specifically to the upper boundary at $(z/l) = 1$, with opposite signs at the lower boundary at $(z/l) = -1$. Figure 14 corresponds to taking the lower signs throughout in equation (A3), together with $t = 0$ and arbitrary phase $\phi = 0$. Complex functions $G(X)$, $F(X)$, and $H(X)$ are given by

$$G(X) = \ln(X - i) \quad F(X) = -i\frac{dG}{dX} \quad H(X) = -\frac{dF}{dX} = i\frac{d^2 G}{dX^2},$$

with real and imaginary parts

$$G_r = \ln\sqrt{X^2 + 1} \quad G_i = \tan^{-1}\left(\frac{-1}{X}\right)$$

$$F_r = \frac{1}{(X^2 + 1)} \quad F_i = \frac{X}{(X^2 + 1)} \quad \text{(A4)}$$

$$H_r = \frac{2X}{(X^2 + 1)^2} \quad H_i = -\frac{(X^2 - 1)}{(X^2 + 1)^2}$$

where we take the signs of numerator and denominator separately in the arctan function in equation (A4) to define the function over the full $360°$ range. We note that the perturbed quantities satisfy div $\boldsymbol{b} = 0$, div $\boldsymbol{j} = 0$, and div $\boldsymbol{u} = 0$, the latter such that the wave flow is incompressible.

[61] Equivalent expressions for the odd modes with $n = 1, 3, 5, \ldots.$ may be obtained from the above simply by interchanging sin and cos in the z functions (not in the Φ functions), switching the signs of b'_x, b'_y, j'_z, i'_x, and i'_y, and noting that the resulting expressions for i'_x and i'_y are valid at both boundaries.

References

Agapitov, O., et al. (2009), Surface waves and field line resonances: A THEMIS case study, *J. Geophys. Res.*, *114*, A00C27, doi:10.1029/2008JA013553.

Anderson, J. D., and G. Schubert (2007), Saturn's gravitational field, internal rotation, and interior structure, *Science*, *317*, 1384–1387.

Andrews, D. J., S. W. H. Cowley, M. K. Dougherty, L. Lamy, G. Provan, and D. J. Southwood (2012), Planetary period oscillations in Saturn's magnetosphere: Evolution of magnetic oscillation properties from southern summer to post-equinox, *J. Geophys. Res.*, *117*, A04224, doi:10.1029/2011JA017444.

Arridge, C. S. et al. (2011), Upstream of Saturn and Titan, *Space. Sci. Rev.*, *162*, 25–83.

Baddeley, L. J., T. K. Yeoman, D. M. Wright, J. A. Davies, K. J. Trattner, and J. L. Roeder (2002), Morning sector drift-bounce resonance driven by ULF waves observed in artificially-induced HF radar backscatter, *Ann. Geophys.*, *20*, 1487–1498.

Baddeley, L. J., T. K. Yeoman, and D. M. Wright (2005), HF Doppler sounder measurements of the ionospheric signatures of small scale ULF waves, *Ann. Geophys.*, *23*, 1807–1820.

Badman, S. V., S. W. H. Cowley, J.-C. Gérard, and D. Grodent (2006), A statistical analysis of the location and width of Saturn's southern auroras, *Ann. Geophys.*, *24*, 3533–3545.

Belenkaya, E. S., S. W. H. Cowley, J. D. Nichols, M. S. Blokhina, and V. V. Kalegaev (2011), Magnetospheric mapping of the dayside UV auroral

oval at Saturn using simultaneous HST images, Cassini IMF data, and a global magnetic field model, *Ann. Geophys.*, 29, 1233–1246.

Branduardi-Raymont, G., P. G. Ford, K. C. Hansen, L. Lamy, A. Masters, B. Cecconi, A. J. Coates, M. K. Dougherty, G. R. Gladstone, and P. Zarka (2013), Search for Saturn's X-ray aurorae at the arrival of a solar wind shock, *J. Geophys. Res.*, 118, doi:10.1002/jgra.50112, in press.

Bunce, E. J., S. W. H. Cowley, C. M. Jackman, J. T. Clarke, F. J. Crary, and M. K. Dougherty (2006), Cassini observations of the interplanetary medium upstream of Saturn and their relation to Hubble Space Telescope auroral data, *Adv. Space Res.*, 38, 806–814.

Bunce, E. J., C. S. Arridge, S. W. H. Cowley, and M. K. Dougherty (2008a), Magnetic field structure of Saturn's dayside magnetosphere and its mapping to the ionosphere: Results from ring-current modeling, *J. Geophys. Res.*, 113, A02207, doi:10.1029/2007JA012538.

Bunce, E. J., et al. (2008b), Origins of Saturn's aurora: Simultaneous observations by Cassini and the Hubble Space Telescope, *J. Geophys. Res.*, 113, A09209, doi:10.1029/2008JA013257.

Burton, M. E., M. K. Dougherty, and C. T. Russell (2010), Saturn's internal planetary magnetic field, *Geophys. Res. Lett.*, 37, L24105, doi:10.1029/2010GL045148.

Carbary, J. F. (2012), The morphology of Saturn's ultraviolet aurora, *J. Geophys. Res.*, 117, A06210, doi:10.1029/2012JA017670.

Cassak, P. A., and A. Otto (2011), Scaling of the magnetic reconnection rate with symmetric shear flow, *Phys. Plasmas*, 18, 074501. doi:10.1063/1.3609771.

Clarke, J. T., et al. (2005), Morphological differences between Saturn's ultraviolet aurorae and those of Earth and Jupiter, *Nature*, 433, 717–719.

Clarke, J. T., et al. (2009), The response of Jupiter's and Saturn's auroral activity to the solar wind, *J. Geophys. Res.*, 114, A05210, doi:10.1029/2008JA013694.

Cowley, S. W. H., E. J. Bunce, and J. M. O'Rourke (2004), A simple quantitative model of plasma flows and currents in Saturn's polar ionosphere, *J. Geophys. Res.*, 109, A05212, doi:10.1029/2003JA010375.

Cowley, S. W. H., C. S. Arridge, E. J. Bunce, J. T. Clarke, A. J. Coates, M. K. Dougherty, J.-C. Gérard, D. Grodent, J. D. Nichols, and D. L. Talboys (2008), Auroral current systems in Saturn's magnetosphere: Comparison of theoretical models with Cassini and HST observations, *Ann. Geophys.*, 26, 2613–2630.

Damiano, P. A., and J. R. Johnson (2012), Electron acceleration in a geomagnetic field line resonance, *Geophys. Res. Lett.*, 39, L02102, doi:10.1029/2011GL050264.

Desroche, M., F. Bagenal, P. A. Delamere, and N. Erkaev (2012), Conditions at the expanded Jovian magnetopause and implications for the solar wind interaction, *J. Geophys. Res.*, 117, A07202, doi:10.1029/2012JA017621.

Dialynas, K., S. M. Krimigis, D. G. Mitchell, D. C. Hamilton, N. Krupp, and P. C. Brandt (2009), Energetic ion spectral characteristics in the Saturnian magnetosphere using Cassini/MIMI measurements, *J. Geophys. Res.*, 114, A01212, doi:10.1029/2008JA013761.

Galand, M., L. Moore, I. Mueller-Wodag, M. Mendillo, and S. Miller (2011), Response of Saturn's auroral ionosphere to electron precipitation: Electron density, electron temperature, and electrical conductivity, *J. Geophys. Res.*, 116, A09306, doi:10.1029/2010JA016412.

Gérard, J.-C., D. Grodent, J. Gustin, A. Saglam, J. T. Clarke, and J. T. Trauger (2004), Characteristics of Saturn's FUV aurora observed with the Space Telescope Imaging Spectrograph, *J. Geophys. Res.*, 109, A09207, doi:10.1029/2004JA010513.

Gérard, J.-C., E. J. Bunce, D. Grodent, S. W. H. Cowley, J. T. Clarke, J. D. Nichols, and S. V. Badman (2005), Signature of Saturn's auroral cusp: Simultaneous Hubble Space Telescope FUV observations and upstream solar wind monitoring, *J. Geophys. Res.*, 110, A11201, doi:10.1029/2005JA011094.

Gérard, J.-C., et al. (2006), Saturn's auroral morphology and activity during quiet magnetospheric conditions, *J. Geophys. Res.*, 111, A12210, doi:10.1029/2006JA011965.

Gérard, J.-C., B. Bonfond, J. Gustin, D. Grodent, J. T. Clarke, D. Bisikalo, and V. Shematovich (2009), Altitude of Saturn's aurora and its implications for the characteristic energy of precipitated electrons, *Geophys. Res. Lett.*, 36, L02202, doi:10.1029/2008GL036554.

Grodent, D., J.-C. Gérard, S. W. H. Cowley, E. J. Bunce, and J. T. Clarke (2005), Variable morphology of Saturn's southern ultraviolet aurora, *J. Geophys. Res.*, 110, A07215, doi:10.1029/2004JA010983.

Grodent, D., A. Radioti, B. Bonfond, and J.-C. Gérard (2010), On the origin of Saturn's outer auroral emission, *J. Geophys. Res.*, 115, A08219, doi:10.1029/2009JA014901.

Grodent, D., J. Gustin, J.-C. Gérard, A. Radioti, B. Bonfond, and W. R. Pryor (2011), Small-scale structure in Saturn's ultraviolet aurora, *J. Geophys. Res.*, 116, A09225, doi:10.1029/2011JA016818.

Hamlin, D. A., R. Karplus, R. C. Vik, and M. Watson (1961), Mirror and azimuthal drift frequencies for geomagnetically trapped particles, *J. Geophys. Res.*, 66, 1–4.

Hughes, W. J., D. J. Southwood, B. Mauk, R. L. McPherron, and J. N. Barfield (1978), Alfvén waves driven by an inverted plasma energy distribution, *Nature*, 275, 43–44.

Kanani, S. J., et al. (2010), A new form of Saturn's magnetopause using a dynamic pressure balance model, based on in situ, multi-instrument Cassini measurements, *J. Geophys. Res.*, 115, A06207, doi:10.1029/2009JA014262.

Kellett, S., C. S. Arridge, E. J. Bunce, A. J. Coates, S. W. H. Cowley, M. K. Dougherty, A. M. Persoon, N. Sergis, and R. J. Wilson (2011), Saturn's ring current: Local time dependence and temporal variability, *J. Geophys. Res.*, 116, A05220, doi:10.1029/2010JA016216.

Kleindienst, G., K.-H. Glassmeier, S. Simon, M. K. Dougherty, and N. Krupp (2009), Quasiperiodic ULF-pulsations in Saturn's magnetosphere, *Ann. Geophys.*, 27, 885–894.

La Belle-Hamer, A. L., A. Otto, and L. C. Lee (1995), Magnetic reconnection in the presence of sheared flow and density asymmetry: Application to the Earth's magnetopause, *J. Geophys. Res.*, 100, 11,875–10,889.

Masters, A., et al. (2010), Cassini observations of a Kelvin-Helmholtz vortex in Saturn's outer magnetosphere, *J. Geophys. Res.*, 115, A07225, doi:10.1029/2010JA015351.

Masters, A., N. Achilleos, J. C. Cutler, A. J. Coates, M. K. Dougherty, and G. H. Jones (2012a), Surface waves on Saturn's magnetopause, *Planet. Space Sci.*, 65, 109–121.

Masters, A., J. P. Eastwood, M. Swisdak, M. F. Thomsen, C. T. Russell, N. Sergis, F. J. Crary, M. K. Dougherty, A. J. Coates, and S. M. Krimigis (2012b), The importance of plasma β conditions for magnetic reconnection at Saturn's magnetopause, *Geophys. Res. Lett.*, 39, L08103, doi:10.1029/2012GL051372.

Maybhate, A., and A. Armstrong (2010), *ACS Instrument Handbook*, Space Telescope Sci. Inst, Baltimore, Md.

McAndrews, H. J. et al. (2009), Plasma in Saturn's nightside magnetosphere and the implications for global circulation, *Planet. Space Sci.*, 57, 1714–1722.

Milan, S. E., N. Sato, M. Ejiri, and J. Moen (2001), Auroral forms and the field-aligned current structures associated with field line resonance, *J. Geophys. Res.*, 106, 25,825–25,833.

Nichols, J. D., J. T. Clarke, S. W. H. Cowley, J. Duval, A. J. Farmer, J.-C. Gérard, D. Grodent, and S. Wannawichian (2008), The oscillation of Saturn's southern auroral oval, *J. Geophys. Res.*, 113, A11205, doi:10.1029/2008JA013444.

Nichols, J. D., et al. (2009), Saturn's equinoctial auroras, *Geophys. Res. Lett.*, 36, L24102, doi:10.1029/2009GL0401491.

Nichols, J. D., B. Cecconi, J. T. Clarke, S. W. H. Cowley, J.-C. Gérard, A. Grocott, D. Grodent, L. Lamy, and P. Zarka (2010a), Variation of Saturn's UV aurora with SKR phase, *Geophys. Res. Lett.*, 37, L15102, doi:10.1029/2010GL044057.

Nichols, J. D., S. W. H. Cowley, and L. Lamy (2010b), Dawn-dusk oscillation of Saturn's conjugate auroral ovals, *Geophys. Res. Lett.*, 37, L24102, doi:10.1029/2010GL045818.

Owen, C. J., and S. W. H. Cowley (1987), A note on current sheet stress balance in the geomagnetic tail for asymmetrical tail lobe plasma conditions, *Planet. Space Sci.*, 35, 467–474.

Radioti, A., D. Grodent, J.-C. Gérard, E. Roussos, C. Paranicas, B. Bonfond, D. G. Mitchell, N. Krupp, S. Krimigis, and J. T. Clarke (2009), Transient auroral features at Saturn: Signatures of energetic particle injections in the magnetosphere, *J. Geophys. Res.*, 114, A03201, doi:10.1029/2008JA013632.

Radioti, A., D. Grodent, J.-C. Gérard, S. E. Milan, B. Bonfond, J. Gustin, and W. Pryor (2011), Bifurcations of the main auroral ring at Saturn: Ionospheric signatures of consecutive reconnection events at the magnetopause, *J. Geophys. Res.*, 116, A11209, doi:10.1029/2011JA016661.

Rae, I. J., et al. (2005), Evolution and characteristics of global Pc5 ULF waves during a high solar wind speed interval, *J. Geophys. Res.*, 110, A12211, doi:10.1029/2005JA011007.

Read, P. L., T. E. Dowling, and G. Schubert (2009), Saturn's rotation period from its atmospheric planetary-wave configuration, *Nature*, 460, 608–610.

Richardson, J. D. (1995), An extended plasma model for Saturn, *Geophys. Res. Lett.*, 22, 1177–1180.

Scoffield, H. C., T. K. Yeoman, D. M. Wright, S. E. Milan, A. N. Wright, and R. J. Strangeway (2007), An investigation of the field aligned currents associated with a large scale ULF wave in the morning sector, *Planet. Space Sci.*, 55, 770–791.

Southwood, D. J. (1974), Some features of field line resonances in the magnetosphere, *Planet. Space Sci.*, 22, 483–491.

Southwood, D. J. (1978), Magnetopause Kelvin-Helmholtz instability, in *Magnetospheric Boundary Layers*, edited by B. Battrick, and J. Mort, pp. 357–364, ESA SP-148, European Space Agency, Paris.

Southwood, D. J., and W. J. Hughes (1983), Theory of hydromagnetic waves in the magnetosphere, *Space Sci. Rev.*, *35*, 301–366.

Southwood, D. J., and M. G. Kivelson (1982), Charged particle behavior in low-frequency geomagnetic pulsations, 2. Graphical approach, *J. Geophys. Res.*, *87*, 1707–1710.

Southwood, D. J., J. W. Dungey, and R. J. Etherington (1969), Bounce resonant interactions between pulsations and trapped particles, *Planet. Space Sci.*, *17*, 349–361.

Stahara, S. S., R. R. Rachiele, J. R. Spreiter, and J. A. Slavin (1989), A three dimensional gasdynamic model for solar wind flow past nonaxisymmetric magnetospheres: Application to Jupiter and Saturn, *J. Geophys. Res.*, *94*, 13,353–13,365.

Thomsen, M. F., D. B. Reisenfeld, D. M. Delapp, R. L. Tokar, D. T. Young, F. J. Crary, E. C. Sittler, M. A. McGraw, and J. D. Williams (2010), Survey of ion plasma parameters in Saturn's magnetosphere, *J. Geophys. Res.*, *115*, A10220, doi:10.1029/2010JA015267.

Wilson, R. J., R. L. Tokar, and M. G. Henderson (2009), Thermal ion flow in Saturn's inner magnetosphere measured by the Cassini plasma spectrometer: A signature of the Enceladus torus? *Geophys. Res. Lett.*, *36*, L23104, doi:10.1029/2009GL040225.

Wilson, R. J., P. A. Delamere, F. Bagenal, and A. Masters (2012), Kelvin-Helmholtz instability at Saturn's magnetopause: Cassini ion data analysis, *J. Geophys. Res.*, *117*, A03212, doi:10.1029/2011JA016723.

Wright, A. N., and W. Allan (1996), Structure, phase motion, and heating within Alfvén resonances, *J. Geophys. Res.*, *101*, 17,399–17,408.

Wright, D. M., T. K. Yeoman, I. J. Rae, J. Storey, A. B. Stockton-Chalk, J. L. Roeder, and K. J. Trattner (2001), Ground-based and Polar spacecraft observations of a giant (Pg) pulsation and its associated source mechanism, *J. Geophys. Res.*, *106*, 10,837–10,852.

Yeoman, T. K., and D. M. Wright (2001), ULF waves with drift resonance and drift-bounce resonance energy sources as observed in artificially-induced HR radar backscatter, *Ann. Geophys.*, *19*, 159–170.

Zieger, B., and K. C. Hansen (2008), Statistical validation of a solar wind propagation model from 1 to 10 AU, *J. Geophys. Res.*, *117*, A08107, doi:10.1029/2008JA013046.